PROCEEDINGS A

royalsocietypublishing.org/journal/rspa

Research

Cite this article: Sucu E, Sakallı I. 2026 Quantum-corrected thermodynamics and plasma-influenced gravitational lensing in Einstein–Euler–Heisenberg black holes. *Proc. R. Soc. A* **482**: 20250936.
https://doi.org/10.1098/rspa.2025.0936

Received: 28 October 2025
Accepted: 5 March 2026

Subject Areas:
astrophysics, high-energy physics, thermodynamics

Keywords:
Einstein–Euler–Heisenberg black holes, generalized uncertainty principle, exponential entropy corrections, plasma gravitational lensing, Gauss–Bonnet theorem

Author for correspondence:
İzzet Sakallı
e-mail: izzet.sakalli@emu.edu.tr

Quantum-corrected thermodynamics and plasma-influenced gravitational lensing in Einstein–Euler–Heisenberg black holes

Erdem Sucu and İzzet Sakallı

Physics Department, Eastern Mediterranean University, North Cyprus, via Mersin 10, Famagusta 99628, Turkey

ES, 0009-0000-3619-1492; IS, 0000-0001-7827-9476

We investigate the thermodynamic properties and gravitational lensing characteristics of black holes (BHs) described by Einstein–Euler–Heisenberg (EEH) nonlinear electrodynamics (NLED), incorporating quantum gravitational corrections and plasma dispersion effects. The spacetime geometry exhibits charge-dependent modifications through coupling constants (α, β) that encode quantum electrodynamical (QED) vacuum polarization, producing distinctive deviations from classical Reissner–Nordström (RN) solutions. We derive the Hawking temperature using a topological approach based on the Euler characteristic, demonstrating how NLED interactions systematically modify the thermal emission spectrum, while the incorporation of generalized uncertainty principle (GUP) corrections introduces a minimal measurable length that suppresses the temperature at small scales and suggests stable Planck-mass remnant formation. Gravitational lensing is analysed via the Gauss–Bonnet theorem (GBT) in both vacuum and plasma environments, revealing how magnetic charge and nonlinear couplings alter photon trajectories through modifications of the optical geometry, with plasma-induced dispersion introducing frequency-dependent corrections that amplify with increasing magnetic charge and produce asymmetric lensing patterns observable through multifrequency radio measurements.

THE ROYAL SOCIETY PUBLISHING

We introduce exponential corrections (ECs) to the Bekenstein–Hawking entropy and examine their effect on thermodynamic stability, deriving modified free energies, pressure, enthalpy and heat capacity that exhibit phase transitions and critical behaviour, while the Joule–Thomson analysis reveals multiple inversion points, where the system switches between cooling and heating regimes under isenthalpic expansion. Our study establishes a testable framework for exploring quantum-corrected BH physics.

1. Introduction

Black holes (BHs) can be described as thermodynamic systems with entropy, temperature and specific heat [1–3]. The correspondence between BH mechanics and thermodynamics, established by Bekenstein and Hawking, reveals deep connections between gravitational dynamics, statistical mechanics and quantum field theory in curved spacetime [4,5]. However, classical Maxwell electromagnetism becomes inadequate when strong fields, vacuum polarization or quantum electrodynamical (QED) effects dominate. The Einstein–Euler–Heisenberg (EEH) theory [6–13] extends the Einstein–Maxwell framework with nonlinear electrodynamics (NLED) corrections encoded in coupling constants (α, β) that capture higher-order QED vacuum fluctuations [14–16]. These interactions arise from one-loop effective actions in QED and represent leading quantum corrections to photon–photon scattering in strong fields [17,18]. Unlike previous studies focusing solely on either thermodynamic or optical aspects of the NLED BHs, the present work provides a unified treatment of EEH BHs by simultaneously incorporating topological Hawking temperature, generalized uncertainty principle (GUP) corrections, plasma-influenced gravitational lensing and exponential entropy modifications. This combined framework enables a self-consistent exploration of quantum-corrected thermodynamics and photon dynamics within a single geometric setting.

The resulting spacetime geometry deviates from the classical Reissner–Nordström (RN) BH spacetime, yielding distinctive thermodynamic and optical properties. The EEH framework has observational implications through lensing asymmetries or shadow deformations of magnetically dominated objects such as magnetars, supermassive BHs or hypothetical magnetic monopoles [19–21]. These signatures make it useful for testing NLED effects in Event Horizon Telescope or Square Kilometre Array observations [22–24]. While magnetic charge Q_m is not directly observable due to the absence of magnetic monopoles, it provides a valuable tool for exploring electromagnetic effects in strong-field regimes.

The EEH model captures quantum corrections at the effective action level, bridging general relativity and quantum gravity [25,26]. Using topological techniques based on the Euler characteristic and Gauss–Bonnet theorem (GBT), the Hawking temperature can be derived independently from the metric ansatz [27,28], recasting temperature calculation as a Ricci scalar integral over a two-dimensional Euclidean section.

Quantum gravity theories predict a minimal measurable length, leading to modifications near BH horizons [29–32]. These modifications, framed through the GUP [30,33–51], reduce the Hawking temperature and suggest remnant formation, providing natural singularity regularization.

Gravitational lensing precisely investigates spacetime geometry and constrains deviations from general relativity [52–56]. Within the GBT framework, light deflection becomes a topological invariant of the optical manifold [57]. In astrophysical contexts, plasma media from accretion discs or stellar winds produce frequency-dependent refractive effects that alter lensing properties [58–60]. The interplay of NLED, plasma dispersion and spacetime curvature enables probing quantum-modified gravity through deflection angles, time delays and shadow deformations [61–73].

Exponential corrections (ECs) to Bekenstein–Hawking entropy allow unified analysis of stability regimes in NLED BHs [74–76]. These quantum corrections encode microstructural information and modify all thermodynamic quantities. Joule–Thomson analysis provides insight

into isenthalpic behaviour in extended phase space [77–80], revealing critical phenomena analogous to van der Waals fluids.

The manuscript is organized to present all thermodynamic content before gravitational lensing, following an astrophysically motivated sequence. Section 2 presents the EEH BH spacetime, derives the metric function, catalogs horizon structures and computes the Hawking temperature using topological methods, followed by GUP corrections. Section 3 introduces ECs to the entropy and derives the complete set of modified thermodynamic quantities, including free energies, pressure, enthalpy and heat capacity. Section 4 presents the Joule–Thomson analysis in extended phase space. With the thermodynamic framework established, §5 analyses vacuum light deflection via the GBT. Section 6 extends lensing to plasma environments. Section 7 summarizes findings and outlines future directions.

2. Black hole spacetime in the Einstein–Euler–Heisenberg theory

The EEH theory extends classical electromagnetism when QED vacuum polarization effects become significant in strong electromagnetic fields [81]. Unlike the linear Maxwell theory, the EEH framework incorporates nonlinear corrections encoding the quantum electromagnetic field nature. These corrections are relevant near compact objects like magnetars and BHs, where magnetic fields can exceed the Schwinger limit $B_c \sim 10^{13}$ G [82]. The resulting spacetime deviates from classical RN BHs, exhibiting modified thermodynamic properties and observational signatures testable with instruments like the Event Horizon Telescope.

In the Einstein frame, the action describing NLED interactions coupled to gravity is [83]

$$\mathcal{S} = \frac{1}{16\pi}\int d^4x\sqrt{-g}[R - \mathrm{e}^{-2\phi}\mathcal{F}^2 - 2\nabla_\mu\phi\nabla^\mu\phi - f(\phi)(2\alpha\,\mathcal{F}^\alpha{}_\beta\mathcal{F}^\beta{}_\gamma\mathcal{F}^\gamma{}_\delta\mathcal{F}^\delta{}_\alpha - \beta\mathcal{F}^4)], \tag{2.1}$$

where R is the Ricci scalar, $\mathcal{F}_{\mu\nu} = \partial_\mu A_\nu - \partial_\nu A_\mu$ is the electromagnetic field strength, $\mathcal{F}^2 = \mathcal{F}_{\mu\nu}\mathcal{F}^{\mu\nu}$ and $\mathcal{F}^4 = \mathcal{F}_{\mu\nu}\mathcal{F}^{\mu\nu}\mathcal{F}_{\alpha\beta}\mathcal{F}^{\alpha\beta}$. The constants α and β are coupling parameters encoding QED vacuum fluctuations. The scalar field ϕ represents the dilaton coupled through $f(\phi)$.

The field equations are

$$G_{\mu\nu} = 2\partial_\mu\phi\partial_\nu\phi - g_{\mu\nu}(\partial\phi)^2 + 2\,\mathrm{e}^{-2\phi}\left(\mathcal{F}_\mu{}^\alpha\mathcal{F}_{\nu\alpha} - \frac{1}{4}g_{\mu\nu}\mathcal{F}^2\right) + f(\phi)\{\cdots\}, \tag{2.2}$$

$$4\Box\phi = -2\,\mathrm{e}^{-2\phi}\mathcal{F}^2 + \frac{\mathrm{d}f(\phi)}{\mathrm{d}\phi}(2\alpha\mathcal{F}^\alpha{}_\beta\mathcal{F}^\beta{}_\gamma\mathcal{F}^\gamma{}_\delta\mathcal{F}^\delta{}_\alpha - \beta\mathcal{F}^4) \tag{2.3}$$

and

$$\partial_\mu\left[\sqrt{-g}(4\mathcal{F}^{\mu\nu}(2\beta f(\phi)\mathcal{F}^2 - \mathrm{e}^{-2\phi}) - 16\alpha\mathcal{F}^\mu{}_\kappa\mathcal{F}^\kappa{}_\lambda\mathcal{F}^{\nu\lambda})\right] = 0. \tag{2.4}$$

For static, spherically symmetric configurations, we adopt

$$\mathrm{d}s^2 = -B(r)\,\mathrm{d}t^2 + \frac{\mathrm{d}r^2}{B(r)} + r^2\,\mathrm{d}\Omega^2, \tag{2.5}$$

with electromagnetic potential

$$A_\mu = (V(r), 0, 0, Q_m\cos\theta), \tag{2.6}$$

where Q_m denotes the magnetic charge.

For a purely magnetic configuration ($V(r) = 0$) and vanishing scalar field ($\phi = 0, f(\phi) = 1$), the exact EEH BH solution is [81]

$$B(r) = 1 - \frac{2M}{r} + \frac{Q_m^2}{r^2} + \frac{2(\alpha-\beta)Q_m^4}{5r^6}. \tag{2.7}$$

This exhibits characteristic departure from RN BHs through the r^{-6} term encoding NLED corrections. The combination $(\alpha - \beta)$ determines whether this correction enhances or diminishes gravitational attraction.

The event horizon radius r_h is determined by the condition $B(r_h) = 0$, which, depending on the values of the NLED parameters, may admit multiple real positive roots corresponding to outer

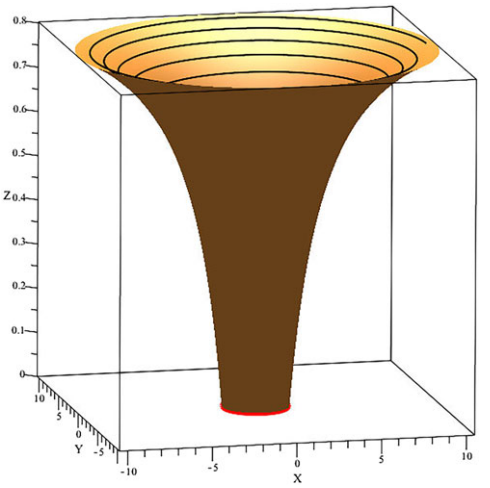

Figure 1. Three-dimensional embedding diagram of an EEH BH spacetime with magnetic charge $Q_m = 0.5$, mass $M = 1$ and nonlinear coupling constants $\alpha = 0.1$, $\beta = 0.1$. The funnel-shaped surface represents the curved geometry near the event horizon, located at $r_h \approx 1.87$. The trajectory illustrates a test particle falling toward the horizon. The throat narrows as the horizon is approached, visualizing the increasing curvature induced by the combined gravitational and NLED effects. Compared to the Schwarzschild case ($Q_m = 0$), the magnetic charge reduces the horizon radius and deepens the potential well.

Table 1. Horizon structures for varying (Q_m, α, β) values.

Q_m	α	β	horizon(s)	configuration
0.0	0.0	0.0	(2.0)	single root BH
0.0	0.0	0.05	(2.0)	single root BH
0.0	0.01	0.0	(2.0)	single root BH
0.0	0.01	0.05	(2.0)	single root BH
0.1	0.0	0.0	(1.994 987 4)	single root BH
0.1	0.0	0.05	(1.994 987 5)	single root BH
0.1	0.01	0.0	(0.047 020 459, 1.994 987 4)	non-extremal BH
0.1	0.01	0.05	(1.994 987 5)	single root BH
0.5	0.0	0.0	(0.133 974 60, 1.866 025 4)	non-extremal BH
0.5	0.0	0.05	(1.866 084 9)	single root BH
0.5	0.01	0.0	(0.210 660 37, 1.866 013 5)	non-extremal BH
0.5	0.01	0.05	(1.866 073 0)	single root BH

and inner (Cauchy) horizons. Solving $B(r_h) = 0$ from equation (2.7) for the ADM mass yields

$$M = \frac{r_h}{2}\left(1 + \frac{Q_m^2}{r_h^2} + \frac{2(\alpha - \beta)Q_m^4}{5r_h^6}\right), \tag{2.8}$$

which relates the constant mass parameter to the horizon radius and the BH charges. This expression is valid only at the horizons and should not be interpreted as a radial function. Table 1 lists horizon configurations for various (Q_m, α, β) with $M = 1$ (figures 1 and 2).

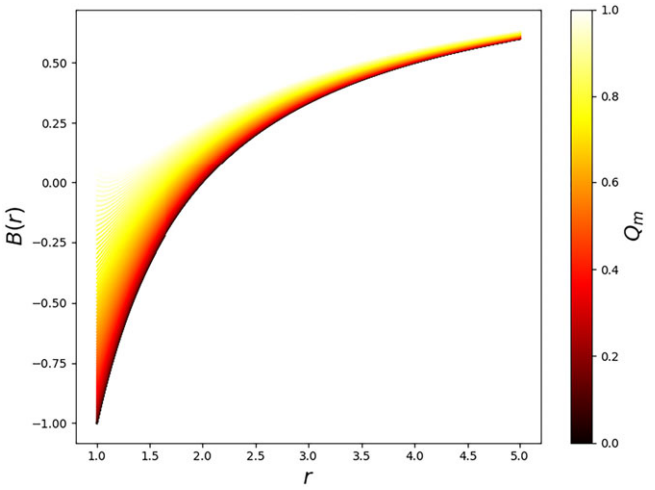

Figure 2. Metric function $B(r)$ for the EEH BH with $M = 1$, $\alpha = 0.3$, $\beta = 0.1$, shown as a function of radial coordinate r and magnetic charge Q_m (colour scale). The horizon location corresponds to $B(r_h) = 0$. For $Q_m = 0$ (bottom of colour scale), the Schwarzschild horizon at $r_h = 2M = 2$ is recovered. As Q_m increases, the outer horizon shifts inward while an inner (Cauchy) horizon emerges at smaller r. The nonlinear EEH correction term $\propto(\alpha - \beta)Q_m^4/r^6$ becomes significant near the horizon, distinguishing this solution from the standard RN case.

(a) A topological framework for computing the global Hawking temperature of Einstein–Euler–Heisenberg black holes

The Hawking temperature can be obtained via a topological approach using the Euclidean geometry of a reduced two-dimensional spacetime [27,28,84]. This GBT-based method provides a coordinate-independent derivation highlighting the geometric underpinnings of BH thermodynamics. The temperature is expressed as

$$T_H = \frac{1}{4\pi\chi}\sum_{j\leq\chi}\int_{r_{h_j}}\sqrt{|g|}\mathcal{R}\,\mathrm{d}r, \tag{2.9}$$

where $\mathcal{R}$ is the Ricci scalar of the two-dimensional Euclidean section, χ the Euler characteristic and r_{h_j} the jth Killing horizon. Note that this approach does not rely on the surface gravity definition, but instead exploits the global topological properties of Euclideanized spacetime. The Hawking temperature emerges as a topological invariant through the Euler characteristic, ensuring that the result remains insensitive to local coordinate choices and reflects the global geometric structure of the BH manifold.

The Euler characteristic is

$$\chi = \frac{1}{4\pi}\int\sqrt{|g|}\mathcal{R}d^2x = \frac{1}{4\pi}\int_0^\beta \mathrm{d}\tau\int_{r_H}\sqrt{|g|}\mathcal{R}\,\mathrm{d}r, \tag{2.10}$$

where Wick rotation $t \to i\tau$ introduces periodic Euclidean time with period $\beta = 1/T_H$. This yields

$$\frac{1}{4\pi T_H}\int_{r_H}\sqrt{|g|}\mathcal{R}\,\mathrm{d}r = \chi, \tag{2.11}$$

leading to equation (2.9).

For the reduced metric

$$\mathrm{d}s^2 = B(r)\,\mathrm{d}\tau^2 + \frac{\mathrm{d}r^2}{B(r)}, \tag{2.12}$$

the Ricci scalar is $\mathcal{R} = -B''(r)$. Integrating yields the global Hawking temperature,

$$T_H = \frac{M}{2\pi r_h^2} - \frac{Q_m^2}{2\pi r_h^3} + \frac{3Q_m^4\alpha}{5\pi r_h^7} - \frac{3Q_m^4\beta}{5\pi r_h^7}. \tag{2.13}$$

The r_h^{-7} terms reflect NLED corrections, demonstrating how quantum field-theoretic effects manifest as modifications to thermodynamic observables.

(b) Emergence of minimal length effects in near-horizon quantum dynamics

Quantum gravitational effects require introducing a minimal measurable length, predicted by string theory and loop quantum gravity [85–88]. At the Planck scale, quantum fluctuations become comparable to classical curvature, breaking down precise localization. The GUP captures this limitation phenomenologically, extending the Heisenberg relation [89–91].

The GUP modifies the canonical uncertainty relation [33]

$$\Delta x \Delta p \geq \hbar \left(1 + \lambda^2 \frac{l_p^2}{\hbar^2}(\Delta p)^2\right), \tag{2.14}$$

where λ is a dimensionless parameter characterizing quantum gravity corrections and $l_p = \sqrt{G\hbar/c^3}$ is the Planck length. The dimensionless parameter λ controls the strength of quantum gravity effects and determines the onset scale at which deviations from the standard uncertainty relation become significant. In the semiclassical limit $\lambda \to 0$, the conventional Hawking temperature is recovered, whereas finite λ values encode minimal length effects that suppress high-energy modes near the horizon. The quadratic term reflects that precise momentum measurements require higher energies, triggering quantum gravitational effects.

Solving for Δp yields

$$\Delta p \simeq \frac{\hbar}{\Delta x}\left(1 + \frac{\lambda^2 l_p^2}{(\Delta x)^2}\right). \tag{2.15}$$

This imposes a lower bound $\Delta x \sim \lambda l_p$, preventing localization below the Planck length and regularizing ultraviolet divergences.

Near the horizon, with $\Delta x \sim 2r_h$, the energy uncertainty becomes [33]

$$\omega_{\mathrm{GUP}} \simeq \omega\left(1 + \frac{\lambda^2 l_p^2}{4r_h^2}\right), \tag{2.16}$$

where ω is the semiclassical energy. For small horizons, GUP corrections dominate the emission spectrum.

In the tunneling picture, emission probability is

$$\Gamma \propto \exp\left[-\frac{4\pi\omega_{\mathrm{GUP}}}{f'(r_h)}\right], \tag{2.17}$$

yielding the GUP-modified temperature

$$T_{\mathrm{GUP}} = \frac{f'(r_h)}{4\pi}\left(1 + \frac{\lambda^2 l_p^2}{4r_h^2}\right)^{-1} = T_H\left(1 - \frac{\lambda^2 l_p^2}{4r_h^2} + \mathcal{O}(l_p^4)\right), \tag{2.18}$$

where T_H is the semiclassical temperature. This suppression suggests remnant formation with characteristic mass $M_{\mathrm{rem}} \sim \sqrt{\lambda} M_{\mathrm{Planck}}$, providing a natural resolution to the information paradox.

For EEH BHs, the GUP-corrected temperature is

$$T_{\mathrm{GUP}}^{\mathrm{EEH}} = \left(\frac{M}{2\pi r_h^2} - \frac{Q_m^2}{2\pi r_h^3} + \frac{3Q_m^4\alpha}{5\pi r_h^7} - \frac{3Q_m^4\beta}{5\pi r_h^7}\right)\left(1 - \frac{\lambda^2 l_p^2}{4r_h^2}\right), \tag{2.19}$$

combining electromagnetic and quantum gravitational effects.

3. Exponential-correction-modified thermodynamics of Einstein–Euler–Heisenberg black holes

The thermodynamic behaviour of BHs extends far beyond classical geometry, displaying rich phase structures and critical features analogous to ordinary matter systems. Although the laws formulated by Bardeen *et al.* [5] establish the fundamental framework, a full description demands quantum corrections—especially significant near the Planck scale. These corrections arise from various quantum gravitational scenarios, including string theory, loop quantum gravity and holographic approaches, each predicting distinct modification patterns that encode information about the underlying microscopic structure of spacetime.

In the semiclassical regime, the entropy satisfies the Bekenstein–Hawking area law,

$$S_0 = \pi r_h^2, \tag{3.1}$$

which links the horizon area to microscopic degrees of freedom through the simple proportionality $S_0 = A_h/(4G\hbar/c^3)$ in units where $\hbar = c = G = 1$. However, as Hawking radiation drives BH evaporation, quantum fluctuations become dominant, invalidating this classical approximation at small scales [92–94].

The holographic principle indicates that quantum gravity introduces additional correction terms—typically logarithmic, inverse or exponential—which encode microstructural information about the horizon degrees of freedom. Among these, ECs capture leading-order quantum effects for small BHs and arise naturally in scenarios where the density of states grows exponentially with the area. Following the statistical–mechanical derivation in [74], the corrected entropy can be expressed as

$$S_{\mathrm{EC}} = S_0 + \mathrm{e}^{-S_0}, \tag{3.2}$$

where the second term represents suppressed quantum contributions that become significant when $S_0 \sim \mathcal{O}(1)$, corresponding to near-Planck-scale horizons. The general quantum-corrected entropy may also include other forms [74],

$$S_{\mathrm{EC}} = S_0 + \alpha \ln g_1(S_0) + \frac{\gamma}{S_0} + \eta\, \mathrm{e}^{g_2(S_0)}, \tag{3.3}$$

with α, γ and η controlling the strength of each correction. In the present work, only the exponential term of equation (3.2) is adopted, with $\mathrm{e}^{-S_0} \approx 1 - S_0 + S_0^2/2$ for moderate entropies.

This modified entropy alters all thermodynamic quantities, introducing systematic shifts in the phase structure and stability criteria of EEH BHs. The corrected internal energy, obtained from the first law of thermodynamics,

$$E_{\mathrm{EC}} = \int T_H \, \mathrm{d}S_{\mathrm{EC}}, \tag{3.4}$$

for the EEH case, gives

$$E_{\mathrm{EC}} \approx \frac{\pi M r_h^2}{2} - \pi Q_m^2 r_h - \frac{2\pi Q_m^4 \alpha}{5 r_h^3} + \frac{2\pi Q_m^4 \beta}{5 r_h^3}. \tag{3.5}$$

Figure 3 illustrates the behaviour of E_{EC} as a function of the horizon radius for $M = 1$, $\alpha = 0.3$ and $\beta = 0.1$ at various magnetic charge values Q_m.

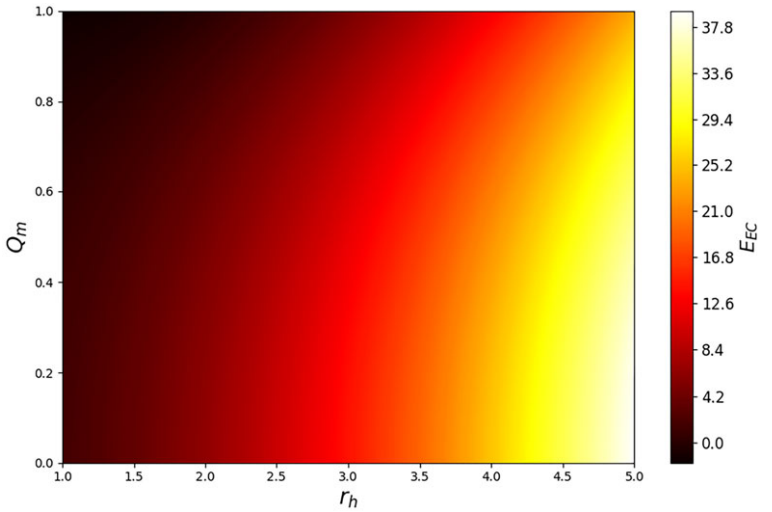

Figure 3. Exponential-corrected internal energy E_{EC} versus horizon radius r_h and magnetic charge Q_m for $M = 1, \alpha = 0.3, \beta = 0.1$. The energy increases monotonically with r_h, reflecting the positive heat capacity regime where larger BHs store more energy. Increasing Q_m raises E_{EC} at fixed r_h due to the electromagnetic field contribution $\propto Q_m^2$. The nonlinear terms $\propto Q_m^4(\alpha - \beta)/r^3$ introduce curvature in the profile at small r_h, where quantum electromagnetic corrections dominate. The exponential entropy correction manifests as a subtle enhancement of energy storage capacity near the Planck scale.

The corresponding Helmholtz free energy, defined as $F_{\mathrm{EC}} = E_{\mathrm{EC}} - T_H S_{\mathrm{EC}}$, reads

$$F_{\mathrm{EC}} \approx \frac{\pi M r_h^2}{4} - \frac{3\pi Q_m^2 r_h}{4} - \frac{7\pi Q_m^4 \alpha}{10 r_h^3} + \frac{7\pi Q_m^4 \beta}{10 r_h^3} + \frac{Q_m^2}{2\pi r_h^3} - \frac{M}{2\pi r_h^2} - \frac{3Q_m^4 \alpha}{5\pi r_h^7} + \frac{3Q_m^4 \beta}{5\pi r_h^7}. \tag{3.6}$$

The Helmholtz free energy serves as the fundamental thermodynamic potential in the canonical ensemble, where the temperature is held fixed. Its minima correspond to thermodynamically stable equilibrium states. Figure 4 displays F_{EC} as a function of r_h for $M = 1$, $\alpha = 0.3$ and $\beta = 0.1$, plotted for multiple Q_m values.

In extended phase space, where the cosmological constant is identified with a thermodynamic pressure $P \sim \Lambda$, the pressure is defined by

$$P_{\mathrm{EC}} = -\frac{\mathrm{d}F_{\mathrm{EC}}}{\mathrm{d}V}, \tag{3.7}$$

leading to

$$P_{\mathrm{EC}} \approx \frac{M}{8r_h} + \frac{3Q_m^2}{16 r_h^2} - \frac{21Q_m^4 \alpha}{40 r_h^6} + \frac{21Q_m^4 \beta}{40 r_h^6} + \frac{3Q_m^2}{8\pi^2 r_h^6} - \frac{M}{4\pi^2 r_h^5} - \frac{21Q_m^4 \alpha}{20\pi^2 r_h^{10}} + \frac{21Q_m^4 \beta}{20\pi^2 r_h^{10}}. \tag{3.8}$$

Figure 5 illustrates the quantum-corrected pressure P_{EC} versus horizon radius for $M = 1$, $\alpha = 0.3$ and $\beta = 0.1$ under different magnetic charge strengths Q_m.

The enthalpy, defined as $H_{\mathrm{EC}} = E_{\mathrm{EC}} + P_{\mathrm{EC}} V$ with $V = 4\pi r_h^3/3$, becomes

$$H_{\mathrm{EC}} \approx \frac{\pi M r_h^2}{3} - \frac{3\pi Q_m^2 r_h}{4} - \frac{11\pi Q_m^4 \alpha}{10 r_h^3} + \frac{11\pi Q_m^4 \beta}{10 r_h^3} - \frac{M}{3\pi r_h^2} + \frac{Q_m^2}{2\pi r_h^3} - \frac{7Q_m^4 \alpha}{5\pi r_h^7} + \frac{7Q_m^4 \beta}{5\pi r_h^7}. \tag{3.9}$$

Figure 6 presents the corrected enthalpy H_{EC} as a function of r_h for $M = 1$, $\alpha = 0.3$ and $\beta = 0.1$.

The Gibbs free energy,

$$G_{\mathrm{EC}} = H_{\mathrm{EC}} - T_H S_{\mathrm{EC}}, \tag{3.10}$$

takes the form

$$G_{\mathrm{EC}} \approx \frac{\pi M r_h^2}{12} - \frac{\pi Q_m^2 r_h}{2} - \frac{7\pi Q_m^4 \alpha}{5 r_h^3} + \frac{7\pi Q_m^4 \beta}{5 r_h^3} + \frac{Q_m^2}{\pi r_h^3} - \frac{5M}{6\pi r_h^2} - \frac{2Q_m^4 \alpha}{\pi r_h^7} + \frac{2Q_m^4 \beta}{\pi r_h^7}. \tag{3.11}$$

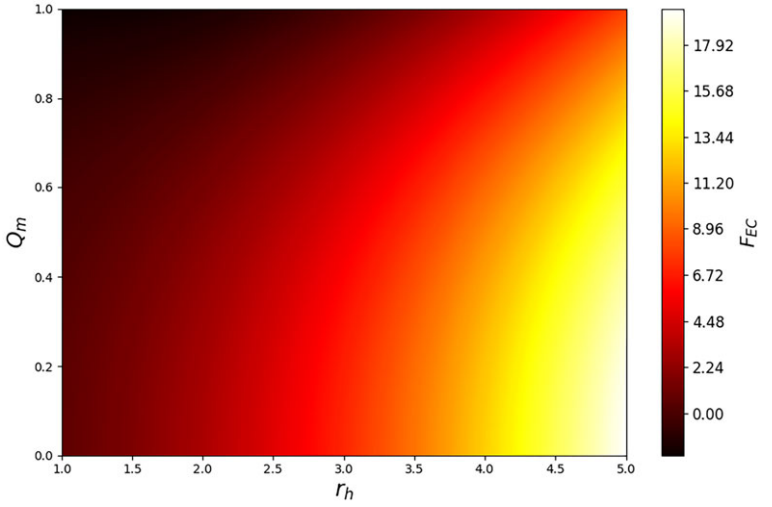

Figure 4. Helmholtz free energy F_{EC} as a function of r_h and Q_m for $M = 1$, $\alpha = 0.3$, $\beta = 0.1$. This thermodynamic potential governs equilibrium in the canonical ensemble (fixed temperature). For small Q_m, a single minimum at intermediate r_h indicates a stable BH phase. As Q_m increases, the minimum shifts toward larger r_h and becomes shallower, suggesting that magnetic repulsion weakens thermodynamic binding and favours larger, more dilute configurations. The EC flattens the free energy landscape at small r_h, raising the cost of forming highly compact states and providing quantum suppression of arbitrarily small horizons.

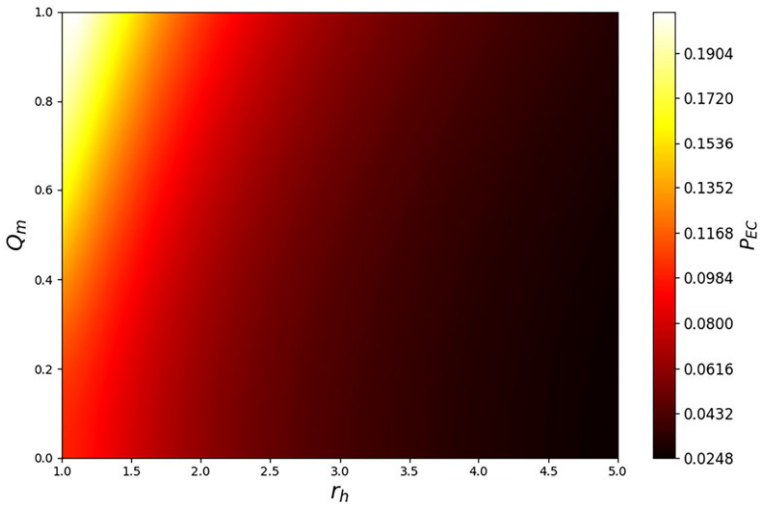

Figure 5. Quantum-corrected pressure P_{EC} versus r_h and Q_m for $M = 1$, $\alpha = 0.3$, $\beta = 0.1$, in extended phase space where $P \sim \Lambda$. The pressure diverges as $r_h \to 0$ in the classical limit, reflecting singular curvature. However, the ECs introduce a regularizing effect that softens this divergence, consistent with quantum gravity resolving classical singularities. Increasing Q_m raises the pressure at fixed r_h due to additional electromagnetic stress-energy. The enhanced high-pressure regime suggests that magnetically charged EEH BHs may exhibit van der Waals-like phase transitions analogous to liquid–gas systems.

The Gibbs free energy serves as the fundamental potential in the grand canonical ensemble, where both temperature and pressure are held fixed. Figure 7 displays G_{EC} versus horizon radius for $M = 1$, $\alpha = 0.3$ and $\beta = 0.1$, under several Q_m configurations.

Finally, the heat capacity, defined as

$$C_{EC} = T_H \left(\frac{\partial S_{EC}}{\partial T_H} \right), \tag{3.12}$$

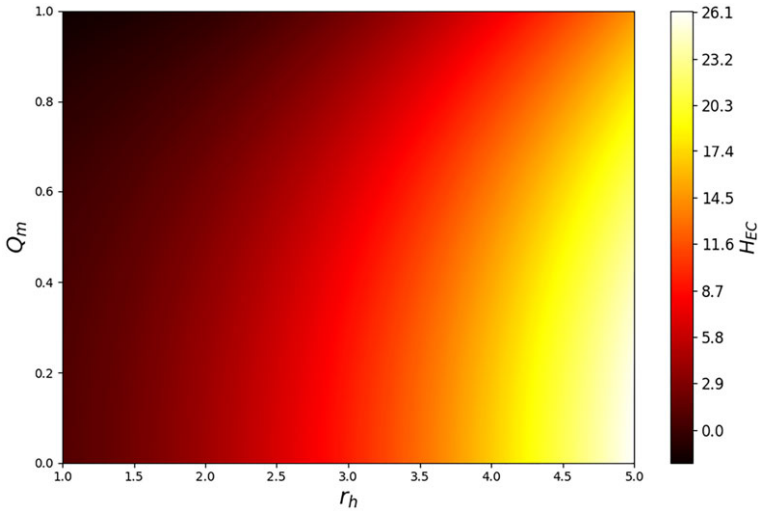

Figure 6. Corrected enthalpy H_{EC} as a function of r_h and Q_m for $M = 1$, $\alpha = 0.3$, $\beta = 0.1$. The enthalpy combines internal energy with pressure–volume work, measuring the total energy accessible during isenthalpic processes. The non-monotonic behaviour—initial increase followed by decline at large r_h—reflects competition between positive mass contribution and negative electromagnetic/quantum correction terms. Increasing Q_m raises the overall enthalpy and delays the onset of decline, indicating that magnetic coupling reinforces energy storage. This quantity governs Joule–Thomson expansion analysed in §4.

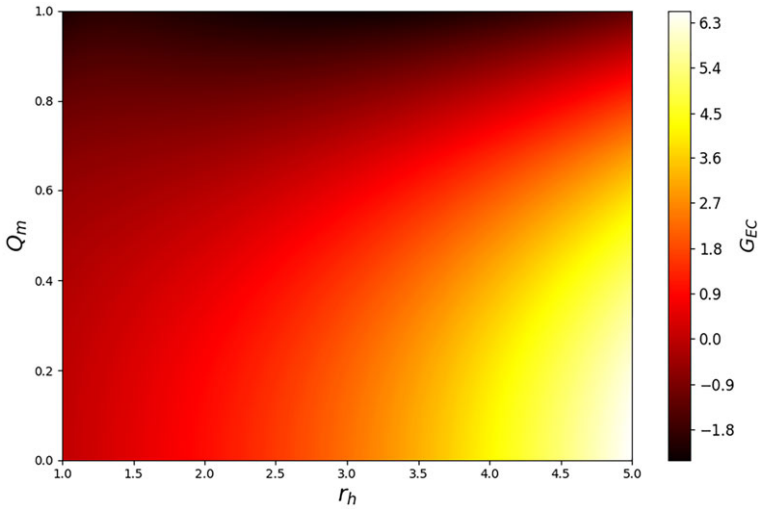

Figure 7. Gibbs free energy G_{EC} versus r_h and Q_m for $M = 1$, $\alpha = 0.3$, $\beta = 0.1$. This potential determines equilibrium in the grand canonical ensemble (fixed T and P). Larger Q_m flattens the Gibbs landscape and shifts transition points toward higher r_h, indicating magnetically induced stabilization of small BH branches. The characteristic swallow-tail structure (visible for certain parameter slices) signals first-order phase transitions where the system jumps discontinuously between small-horizon and large-horizon phases. The ECs modify the relative depth of competing phases, potentially altering the coexistence curve and critical point location.

is found as

$$C_{EC} \approx -\frac{2(6(\alpha-\beta)Q_m^4 - 5Q_m^2 r_h^4 + 5M r_h^5)r_h^4\pi^2}{42(\alpha-\beta)Q_m^4 - 15Q_m^2 r_h^4 + 10M r_h^5}. \tag{3.13}$$

The heat capacity measures the thermal response of the system and signals thermodynamic stability through its sign: $C_{EC} > 0$ indicates stable equilibrium, while $C_{EC} < 0$ signifies instability.

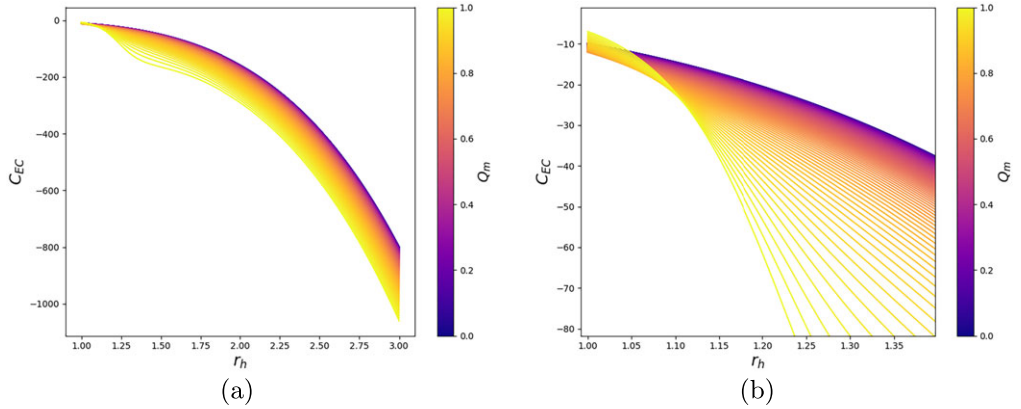

Figure 8. Heat capacity C_{EC} as a function of r_h for $M = 1$, $\alpha = 0.3$, $\beta = 0.1$ at varying Q_m (colour scale). (a) Full range showing multiple stability windows: $C_{EC} > 0$ indicates thermodynamically stable phases, while $C_{EC} < 0$ signals instability. Divergences mark second-order phase transitions where the system switches between stable and unstable branches. (b) Zoomed view of the critical region near $r_h \approx 1.2$, highlighting the intricate transition structure. The divergence locations shift systematically with Q_m, demonstrating that magnetic charge acts as a control parameter tuning critical temperature and horizon radius. The alternating signs across different regions reveal a complex phase diagram characteristic of quantum-corrected BH thermodynamics.

Table 2. Comparison of standard and GUP-corrected Hawking temperature for EEH BH with $M = 1$, $Q_m = 0.5$, $\alpha = 0.3$, $\beta = 0.1$, $\lambda = 1$, $l_p = 0.5$.

r_h	T_H (standard)	T_{GUP} (corrected)	suppression (%)
1.5	0.05909	0.05744	2.78
2.0	0.03483	0.03429	1.56
2.5	0.02292	0.02269	1.00
3.0	0.01621	0.01610	0.69
4.0	0.00933	0.00929	0.39

The divergence points of the heat capacity signal second-order phase transitions, separating stable and unstable thermodynamic branches. The corresponding swallow-tail structure observed in the Gibbs free energy further confirms the presence of first-order phase transitions, analogous to those encountered in van der Waals fluids within extended phase space. Figure 8 displays the heat capacity C_{EC} as a function of horizon radius for $M = 1$, $\alpha = 0.3$ and $\beta = 0.1$ at different Q_m values.

To clarify the physical effect of quantum corrections, we provide explicit numerical comparisons between the corrected and uncorrected thermodynamic quantities.

Tables 2 and 3 demonstrate that quantum corrections become increasingly important as the horizon radius approaches the Planck scale. The GUP-induced temperature suppression reaches 2.78% at $r_h = 1.5$ and grows rapidly for smaller horizons, ultimately driving $T_{GUP} \to 0$ at $r_h = \lambda l_p/2 = 0.25$. Similarly, the exponential entropy correction contributes significantly (more than 1%) only for $r_h \lesssim 1$, encoding microstructural information that becomes relevant during the final stages of BH evaporation. These features—remnant formation and modified entropy at small scales—are entirely absent in the quantum-uncorrected treatment and represent the central novel predictions of our framework.

Table 3. Entropy corrections: Bekenstein–Hawking entropy S_0 versus exponential-corrected entropy S_{EC}. The correction is substantial only for near-Planck-scale horizons.

r_h	$S_0 = \pi r_h^2$	$S_{EC} = S_0 + e^{-S_0}$	correction (%)
0.5	0.7854	1.2413	58.1
0.8	2.0106	2.1445	6.66
1.0	3.1416	3.1848	1.38
1.5	7.0686	7.0694	0.012
2.0	12.566	12.566	2.8×10^{-5}

Table 4. Interplay between EEH parameters and physical observables. Arrows indicate the direction of change when the parameter increases. The symbol '—' denotes no leading-order effect.

Parameter	T_H	Θ	r_h^{crit}	M_{rem}
$(\alpha - \beta) \uparrow$	$\uparrow$	$\downarrow$	$\uparrow$	—
$Q_m \uparrow$	$\downarrow$	$\downarrow$	$\uparrow$	—
$\lambda l_p \uparrow$ (GUP)	$\downarrow$	—	—	$\uparrow$
$\delta \uparrow$ (plasma)	—	$\uparrow$	—	—

(a) Interplay between nonlinear electrodynamics, quantum corrections and topological methods

The EEH framework reveals a deep interconnection between NLED, quantum corrections and the topological methods employed throughout this work. The GBT provides a unified geometric foundation for both thermodynamic and optical analyses:

— *Thermodynamics*. The Hawking temperature emerges from the integral $T_H = (4\pi\chi)^{-1} \int \sqrt{|g|}\mathcal{R}\, dr$, where $\mathcal{R} = -B''(r)$ is the Ricci scalar of the two-dimensional Euclidean section.
— *Gravitational lensing*. The deflection angle derives from $\Theta = -\int K\sqrt{\det g_{opt}}\, dr\, d\phi$, where K is the Gaussian curvature of the optical manifold.

The NLED parameter $(\alpha - \beta)$ enters the metric function through the term $2(\alpha - \beta)Q_m^4/(5r^6)$, which simultaneously determines both curvature quantities. This geometric unity implies that modifications to the electromagnetic sector propagate coherently to all observables derived from spacetime curvature.

Table 4 summarizes how each physical parameter influences the key observables. The responses exhibit characteristic asymmetries that provide potential observational discriminants:

— GUP corrections suppress T_H via the factor $(1 - \lambda^2 l_p^2/4r_h^2)$ but leave the deflection angle unaffected at leading order, since the optical geometry depends only on the background metric.
— Plasma dispersion modifies Θ through the frequency-dependent refractive index but has no influence on BH thermodynamics.
— The NLED parameter $(\alpha - \beta)$ affects both temperature and lensing, enabling combined constraints from thermal emission spectra and gravitational lensing observations.

We note that NLED corrections scale as r_h^{-7} for temperature and b^{-6} for deflection, making them subdominant for large horizons ($r_h \gtrsim 2M$) and impact parameters ($b \gtrsim 5M$). However, these corrections become significant in the strong-field regime: near the photon sphere ($b \sim 3M$) or for small primordial BHs approaching the Planck scale. The exponential entropy correction e^{-S_0} similarly activates only for near-Planck horizons (table 3), providing a natural UV completion to semiclassical thermodynamics.

This unified perspective demonstrates that the EEH framework provides a self-consistent testable theory: thermodynamic measurements (Hawking spectra, phase transitions) and optical measurements (lensing, shadows) probe complementary aspects of the same underlying geometry, with quantum corrections (GUP, ECs) activating at the Planck scale while NLED effects persist at all scales proportional to $Q_m^4(\alpha - \beta)$.

These relations reveal that exponential quantum corrections significantly modify the thermodynamic behaviour and stability of EEH BHs, particularly in the small-horizon regime where quantum effects dominate classical gravity.

4. Quantum-corrected Joule–Thomson analysis for Einstein–Euler–Heisenberg black holes

The Joule–Thomson effect describes an isenthalpic process where the temperature changes with pressure under conditions of constant enthalpy, providing a fundamental probe of thermodynamic stability and phase structure in extended phase-space formulations of BH thermodynamics [95–97]. In ordinary thermodynamic systems, the Joule–Thomson coefficient determines whether a gas cools or heats upon expansion through a throttle, with the sign change occurring at the inversion curve separating these two regimes. For BHs, this framework defines an isenthalpic trajectory in the extended phase space where the cosmological constant is interpreted as a thermodynamic pressure, allowing the investigation of phase transitions and critical phenomena analogous to van der Waals fluids. The incorporation of the ECs to the entropy introduces quantum modifications to the Joule–Thomson behaviour, particularly in the small-horizon regime where quantum gravitational effects become dominant. These corrections reveal how the interplay between NLED interactions, magnetic charge and quantum entropy modifications shapes the thermal response of EEH BHs under isenthalpic expansion or compression.

Starting from the first law of BH thermodynamics in extended phase space, $\mathrm{d}M = T_H\,\mathrm{d}S + V\,\mathrm{d}P + \Phi\,\mathrm{d}Q_m$, where Φ is the electrostatic potential conjugate to the magnetic charge, the BH heat capacity defined in equation (3.13) provides the thermodynamic basis for analysing the Joule–Thomson effect. The heat capacity C_{EC} encodes the isothermal stability of the system and exhibits divergences at critical points where the system undergoes second-order phase transitions. The specific heat computed in equation (3.13) provides the basis for analysing the Joule–Thomson behaviour in the quantum-corrected regime, as it determines the relationship between temperature fluctuations and entropy variations that govern the isenthalpic response.

The Joule–Thomson coefficient, quantifying the temperature response to pressure along an isenthalpic path, is defined as [79,98]

$$\mu_J = \left(\frac{\partial T_H}{\partial P_{\mathrm{EC}}}\right)_H = \frac{\partial T_H}{\partial P_{\mathrm{EC}}}. \tag{4.1}$$

This coefficient measures the rate of temperature change per unit pressure variation while maintaining constant enthalpy H_{EC}, providing a direct diagnostic of the thermodynamic stability and phase behaviour. The sign of μ_J determines the cooling or heating character of the process: $\mu_J > 0$ corresponds to cooling upon expansion (decrease in pressure), while $\mu_J < 0$ indicates heating. The locus of points where $\mu_J = 0$ defines the inversion curve, which separates these two thermodynamic regimes and plays a crucial role in understanding the phase structure of the system.

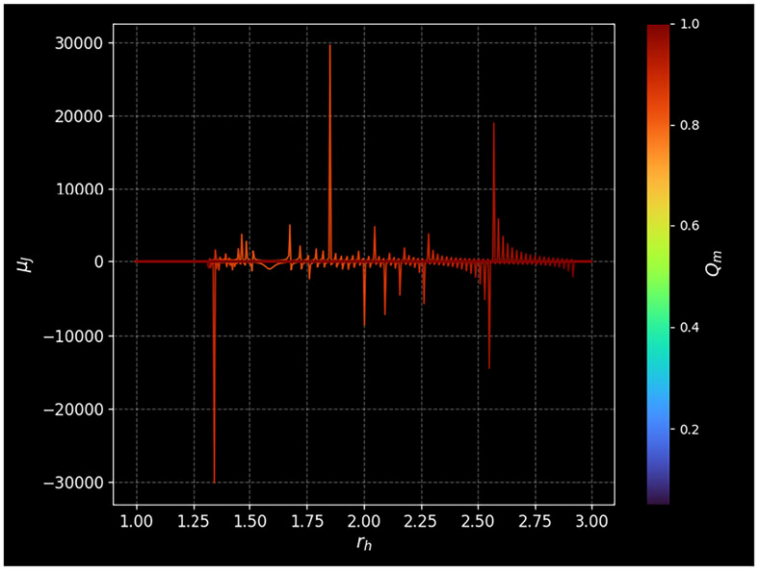

Figure 9. Joule–Thomson coefficient μ_J versus r_h for $M = 1$, $\alpha = 0.3$, $\beta = 0.1$ at varying Q_m (colour scale). This coefficient quantifies temperature change under isenthalpic expansion: $\mu_J > 0$ indicates cooling (temperature decreases with pressure), while $\mu_J < 0$ indicates heating. The multiple sign changes and divergences reveal a rich phase structure with transitions between cooling-dominated and heating-dominated regimes. Inversion points ($\mu_J = 0$) align with heat capacity divergences in figure 8, confirming thermodynamic consistency. Increasing Q_m shifts inversion points toward larger r_h and modifies the coefficient amplitude. At large r_h, $\mu_J \to 0$, recovering the classical limit where quantum corrections become negligible.

Using the chain rule and the implicit function theorem applied to the constraint $H_{\rm EC}(T_H, P_{\rm EC}, r_h) = \text{constant}$, the Joule–Thomson coefficient can be expressed in terms of the quantities X and Y as

$$\mu_J = -\frac{X}{Y}, \tag{4.2}$$

in which

$$X = 4(42(\alpha - \beta)Q_m^4 - 15Q_m^2 r_h^4 + M r_h^5) r_h^3 \pi \tag{4.3}$$

and

$$Y = -126\left(\pi^2 r_h^4 + \frac{10}{3}\right)(\beta - \alpha)Q_m^4 + 15(-\pi^2 r_h^8 - 6r_h^4)Q_m^2 + 5M r_h^5(\pi^2 r_h^4 + 10). \tag{4.4}$$

The numerator X encodes the combined influence of mass, magnetic charge and NLED coupling on the temperature gradient, while the denominator Y captures the corresponding pressure response, including contributions from the exponential entropy correction through the modified thermodynamic relations. The appearance of the combination $(\alpha - \beta)Q_m^4$ in both expressions reflects the fundamental role of the NLED invariants in determining the isenthalpic behaviour, with the relative sign of α and β controlling whether the quantum electromagnetic corrections enhance or suppress the Joule–Thomson effect.

Note that the inversion points of μ_J, defined by $X = 0$, closely follow the heat capacity divergence structure given by the zeros of the denominator in equation (3.13), confirming that the underlying quantum corrections simultaneously regulate both isenthalpic and isothermal instabilities. This correspondence is not accidental but rather reflects a deep thermodynamic consistency: both the heat capacity and the Joule–Thomson coefficient are derived from the same fundamental entropy function $S_{\rm EC}$ and thus share common critical behaviour. The divergences in $C_{\rm EC}$ mark second-order phase transitions where the system switches between thermodynamically stable and unstable branches, while the inversion points of μ_J delineate boundaries in the

extended phase space where the character of the isenthalpic expansion changes qualitatively. The alignment of these structures indicates that the ECs introduce a unified modification to the phase diagram that affects all thermodynamic response functions coherently.

Figure 9 illustrates the Joule–Thomson coefficient μ_J versus horizon radius for $M = 1$, $\alpha = 0.3$ and $\beta = 0.1$ with distinct Q_m values. The plot reveals a complex structure with multiple sign changes and divergences, indicating regions where the BH exhibits cooling ($\mu_J > 0$) or heating ($\mu_J < 0$) under isenthalpic expansion. The colour gradient encodes the magnitude of Q_m, showing that increasing magnetic charge systematically shifts the inversion points toward larger horizon radii and modifies the overall amplitude of the Joule–Thomson coefficient. For small r_h, the coefficient exhibits sharp variations associated with the approach to the quantum regime where ECs become significant. The divergence points visible in the plot correspond to the zeros of the denominator Y in equation (4.4), which coincide with the critical radii where the heat capacity C_{EC} also diverges, as predicted by the thermodynamic consistency requirement. The asymptotic behaviour at large r_h shows that μ_J approaches zero, indicating that the Joule–Thomson effect vanishes in the classical limit where quantum corrections are negligible and the BH behaves like a Schwarzschild solution perturbed by weak electromagnetic fields.

The physical interpretation of the Joule–Thomson behaviour can be elucidated by examining the competing contributions to X and Y. The mass term $\propto M r^8$ in X represents the gravitational binding energy that favours heating upon expansion, as the BH must perform work against its own gravitational field. The magnetic charge term $\propto Q_m^2 r^4$ introduces an electromagnetic contribution that can either enhance or oppose this tendency depending on the balance with the gravitational term. The nonlinear EEH term $\propto(\alpha - \beta)Q_m^4$ adds a quantum electromagnetic correction that modifies the effective equation of state, with the sign of $(\alpha - \beta)$ determining whether the vacuum polarization effects increase or decrease the Joule–Thomson response. The exponential entropy correction enters through the modified thermodynamic potentials and alters the relative weight of these competing effects, particularly at small horizons where the correction term e^{-S_0} becomes comparable to the classical Bekenstein–Hawking entropy S_0.

The presence of multiple inversion points in the μ_J profile suggests a rich phase structure in the extended phase space, with the system transitioning between cooling-dominated and heating-dominated regimes as the horizon radius varies. This behaviour is reminiscent of the inversion curve structure observed in real gases such as nitrogen or methane, where the sign of the Joule–Thomson coefficient depends sensitively on the temperature and pressure due to the interplay between attractive and repulsive intermolecular forces. For EEH BHs, the analogous interplay occurs between gravitational attraction, electromagnetic repulsion, nonlinear QED corrections and quantum gravitational effects, producing a similarly complex phase diagram. Future work could extend this analysis to the critical regime, where the inversion curve intersects the coexistence line, potentially revealing new critical phenomena specific to quantum-corrected BHs in NLED theories.

5. Light deflection in vacuum: Gauss–Bonnet theorem framework for Einstein–Euler–Heisenberg black hole lensing

Gravitational lensing remains one of the most accurate observational signatures of gravitation, probing the validity of gravitational models under various astrophysical conditions [62,99]. Light deflection by compact masses carries information about deviations from general relativity, offering diagnostics for extended theories such as EEH electrodynamics. Modern astrophysical precision—from gravitational wave detectors to Event Horizon Telescope imaging and stellar orbit astrometry near Sagittarius A*—enables strong-field tests where deviations of a few per cent from general relativity can be constrained [54]. Before proceeding, we address an important subtlety: photon propagation in NLED is generally polarization-dependent due to vacuum birefringence. In the EEH framework with purely magnetic configuration, the electromagnetic invariant is $\mathcal{F} = 2Q_m^2/r^4$, and two polarization modes emerge. The ordinary mode follows null

geodesics of $g_{\mu\nu}$, while the extraordinary mode experiences an effective metric modified by $(1 + 8\alpha Q_m^2/r^4)$. In the weak-field regime $b \gg r_h$, the birefringence correction scales as $\mathcal{O}(\alpha Q_m^2/b^2)$, subdominant to the leading gravitational term $4M/b$ when $\alpha Q_m^2 \ll Mb$. Our analysis applies to the ordinary mode; strong-field lensing near the photon sphere would require the full effective metric formalism for both modes, left for future work.

Conventionally, photon bending is obtained through null geodesic integration, which becomes analytically intractable with NLED couplings. The GBT method [57] provides an elegant reformulation by expressing the deflection angle as an integral of Gaussian curvature over the optical geometry. This technique proves efficient for EEH BHs where nonlinearities complicate standard geodesic approaches, recasting the lensing problem as a global topological property of the two-dimensional optical manifold.

Within the GBT formalism, light-bending is interpreted as a global geometric property rather than a local dynamical effect. The deflection angle is expressed as a curvature integral over the domain exterior to the light trajectory, capturing both near-horizon strong-field effects and asymptotic weak-field corrections in a unified framework.

For photon motion in the equatorial plane ($\theta = \pi/2$), with emitter and observer at spatial infinity (thin-lens approximation), the optical metric from the null condition $ds^2 = 0$ is

$$\mathrm{d}t^2 = \frac{1}{B^2(r)}\,\mathrm{d}r^2 + \frac{r^2}{B(r)}\,\mathrm{d}\phi^2, \tag{5.1}$$

defining a two-dimensional Riemannian surface. The coefficients encode gravitational and electromagnetic contributions, making the deflection angle sensitive to both curvature and NLED effects [61,100]. The metric function $B(r)$ from equation (2.7) contains EEH corrections through the term $2(\alpha - \beta)Q_m^4/(5r^6)$. The fundamental quantity is the Gaussian curvature K, related to the Ricci scalar by [84] effect $K = R/2$. In the weak-field domain ($b \gg r_h$), writing $\varepsilon = \alpha - \beta$ and decomposing $K = K_0 + \varepsilon K_\varepsilon + \mathcal{O}(\varepsilon^2)$, one obtains

$$K_0 = \frac{2M}{r^3} + \frac{3(M^2 + Q_m^2)}{r^4} - \frac{6MQ_m^2}{r^5} + \frac{2Q_m^4}{r^6} \tag{5.2}$$

and

$$K_\varepsilon = -\frac{42Q_m^4}{5r^8} + \frac{76MQ_m^4}{5r^9} - \frac{36Q_m^6}{5r^{10}}, \tag{5.3}$$

where K_0 encodes the gravitational and magnetic-charge curvature (RN sector) and K_ε the leading EEH nonlinear correction. The $\mathcal{O}(\varepsilon^2)$ remainder contributes only at Q_m^8/r^{14} and is negligible in the weak-field regime.

This reveals hierarchical corrections: leading Schwarzschild term $\propto M/r^3$, RN magnetic charge correction $\propto Q_m^2/r^4$ and nonlinear EEH terms at higher orders. The combination $(\alpha - \beta)$ appears repeatedly since the nonlinear invariants contribute with opposite signs to the effective electromagnetic energy density.

To obtain the weak-field deflection angle consistently to second order, we employ the Binet orbit equation rather than integrating the Gaussian curvature along the Born (straight-line) path, since the latter is inconsistent beyond first order in M/b and Q_m^2/b^2 [101,102]. The GBT connects the deflection angle with the integral of K over the region outside the photon trajectory,

$$\Theta = -\lim_{R\to\infty} \int_0^{\pi} \int_{b/\sin\phi}^{R} K\sqrt{\det g}\,\mathrm{d}r\,\mathrm{d}\phi, \tag{5.4}$$

where b is the impact parameter and $\sqrt{\det g}$ the metric determinant. However, evaluating this integral along the straight-line path $r = b/\sin\phi$ yields coefficients that are only correct at first order; at second order, orbit corrections to the integration path generate additional contributions that the Born approximation misses. A consistent treatment is provided by the null geodesic

(Binet) equation:

$$\frac{\mathrm{d}^2u}{\mathrm{d}\phi^2}+u=3Mu^2-2Q_m^2u^3-\frac{8(\alpha-\beta)}{5}Q_m^4u^7, \tag{5.5}$$

where $u\equiv 1/r$. We expand perturbatively about the zeroth-order trajectory $u_0=\sin\phi/b$, treating M/b and Q_m^2/b^2 as independent small parameters. The first-order orbit corrections satisfy

$$u_1^{(M)\prime\prime}+u_1^{(M)}=\frac{3M\sin^2\phi}{b^2}\quad\text{and}\quad u_1^{(Q)\prime\prime}+u_1^{(Q)}=-\frac{2Q_m^2\sin^3\phi}{b^3}, \tag{5.6}$$

with boundary conditions $u_1(0)=u_1'(0)=0$. The solutions are

$$u_1^{(M)}=\frac{M(\cos\phi-1)^2}{b^2}\quad\text{and}\quad u_1^{(Q)}=-\frac{Q_m^2}{16b^3}(-12\phi\cos\phi+9\sin\phi+\sin 3\phi). \tag{5.7}$$

The second-order corrections are driven by $F'(u_0)u_1=(6Mu_0-6Q_m^2u_0^2)u_1$, generating three source terms at orders M^2/b^4, MQ_m^2/b^5, and Q_m^4/b^6. Solving the forced oscillator equations and using $\hat{\alpha}=b[u_1(\pi)+u_2(\pi)]$—noting that $u_1^{(M)\prime}(\pi)=u_1^{(Q)\prime}(\pi)=0$, so no cross-term arises—we obtain the vacuum deflection angle ($\hat{\alpha}_{\mathrm{vac}}\equiv\Theta$),

$$\Theta=\frac{4M}{b}-\frac{3\pi Q_m^2}{4b^2}+\frac{15\pi M^2}{4b^2}-\frac{16MQ_m^2}{b^3}+\frac{105\pi Q_m^4}{64b^4}-\frac{7\pi(\alpha-\beta)Q_m^4}{16b^6}+\mathcal{O}(b^{-5}). \tag{5.8}$$

The leading term $4M/b$ reproduces Einstein's prediction for Schwarzschild BHs. The Q_m^2/b^2 term shows that magnetic charge reduces the bending. The M^2/b^2 coefficient $15\pi/4$ recovers the well-known post–post-Newtonian Schwarzschild result [101–103]. The mixed term $-16MQ_m^2/b^3$ and the Q_m^4/b^4 coefficient $105\pi/64$ are new results specific to the magnetically charged EEH geometry. The last term encodes the EEH NLED correction and is already first order in $(\alpha-\beta)$, so no further orbit correction is needed at this order. The deflection can be decomposed into contributions: purely gravitational terms $\propto M$ and M^2; magnetic charge terms $\propto Q_m^2$ and Q_m^4 encoding electromagnetic energy; mixed terms $\propto MQ_m^2$ reflecting gravitational–electromagnetic coupling; and nonlinear terms $\propto(\alpha-\beta)Q_m^4$ representing quantum vacuum polarization corrections. Different astrophysical systems—magnetars, supermassive BHs or primordial BHs—may exhibit distinct lensing signatures depending on their charge-to-mass ratio and NLED interaction strength.

6. Photon deflection in a plasma environment via the Gauss–Bonnet theorem: Einstein–Euler–Heisenberg black hole lensing in astrophysical media

When light propagates through realistic astrophysical environments, the surrounding plasma introduces additional physical effects that significantly alter lensing characteristics compared to the vacuum scenario. Indeed, compact objects are rarely isolated; they are typically enveloped by ionized matter arising from accretion discs, stellar winds or interstellar plasma [104,105]. The presence of plasma is particularly ubiquitous in the vicinity of active galactic nuclei, X-ray binaries, pulsars and magnetars, where high-energy processes ionize the surrounding gas and create dense regions of free electrons. These environments introduce frequency-dependent refractive effects that can significantly modify the observed lensing signatures, potentially masking or enhancing the geometric effects encoded in the underlying spacetime metric. Understanding the interplay between plasma dispersion and gravitational lensing is, therefore, crucial for correctly interpreting observations and extracting fundamental parameters such as the BH mass, charge and the strength of NLED interactions.

In such media, the photon's propagation deviates from null geodesics, as the plasma modifies the effective refractive geometry in a frequency-dependent manner [58]. This modification arises because photons interact with the free charges in the plasma through Compton scattering and collective plasma oscillations, leading to a refractive index that depends on both the local electron density and the photon frequency. To account for this effect around an EEH BH, we again restrict

the motion to the equatorial plane, leveraging the spherical symmetry of the system to reduce the problem to a two-dimensional optical geometry. The medium's impact is captured through the refractive index [64],

$$n(r) = \sqrt{1 - \frac{\omega_e^2}{\omega_\infty^2} f(r)}, \tag{6.1}$$

where ω_e is the local electron plasma frequency and ω_∞ is the photon frequency measured by a distant observer. The plasma frequency $\omega_e = \sqrt{4\pi n_e e^2/m_e}$ is determined by the local electron number density n_e, which may vary radially depending on the density profile of the surrounding medium. This index encapsulates the dispersive nature of electromagnetic propagation in plasma, with its magnitude determined by the local density of free charges. The functional dependence on $f(r) = B(r)$ ensures that the refractive index remains consistent with the underlying spacetime geometry, coupling the plasma dispersion to the gravitational and electromagnetic structure of the EEH BH.

Consequently, the effective optical metric that dictates photon trajectories becomes

$$d\sigma^2 = n^2(r)\left(\frac{dr^2}{f(r)} + r^2\, d\phi^2\right), \tag{6.2}$$

revealing how both curvature and refractive effects shape the geometry of light propagation. The dependence of $n(r)$ on the local plasma parameters introduces a spatially varying optical curvature, which becomes increasingly pronounced in high-density regions near compact sources. In accretion disc environments, for example, the electron density typically peaks near the innermost stable circular orbit and decays as a power law at larger radii, producing a radially dependent refractive index that can lead to chromatic aberration in the lensed images.

The Gaussian curvature of this modified optical manifold governs the geometric deflection in the same way as in a vacuum but now carries explicit plasma contributions. In the weak-field approximation, introducing $\varepsilon = \alpha - \beta$ and decomposing $K = K_0 + \delta K_\delta + \varepsilon K_\varepsilon + \mathcal{O}(\delta\varepsilon)$, the individual contributions read

$$K_0 = \frac{2M}{r^3} + \frac{3(M^2 + Q_m^2)}{r^4} - \frac{6MQ_m^2}{r^5} + \frac{2Q_m^4}{r^6}, \tag{6.3}$$

$$K_\delta = -\frac{3M}{r^3} + \frac{12M^2 + 5Q_m^2}{r^4} - \frac{M(12M^2 + 26Q_m^2)}{r^5} + \frac{32M^2Q_m^2 + 10Q_m^4}{r^6} - \frac{23MQ_m^4}{r^7} + \frac{5Q_m^6}{r^8} \tag{6.4}$$

and

$$K_\varepsilon = -\frac{42Q_m^4}{5r^8} + \frac{76MQ_m^4}{5r^9} - \frac{36Q_m^6}{5r^{10}}, \tag{6.5}$$

where $\delta = \omega_e^2/\omega_\infty^2$ quantifies the plasma dispersion strength, K_0 encodes the gravitational and electromagnetic curvature, K_δ the plasma-induced modifications and K_ε the EEH nonlinear corrections. The mixed $\delta\varepsilon$ terms are suppressed by an additional power of Q_m^4/r^8 and are omitted. For typical astrophysical plasmas, δ ranges from approximately 10^{-10} in tenuous intergalactic media to approximately 10^{-4} in dense accretion disc coronae, making the plasma corrections potentially observable in high-precision astrometry.

As discussed in §5, evaluating the GBT area integral along the straight-line path $r = b/\sin\phi$ (Born approximation) is inconsistent beyond first order. We, therefore, employ the Binet orbit equation, which in the presence of a uniform cold plasma acquires additional source terms proportional to δ [59,105,106]. The plasma contributions to the Binet equation read

$$\Delta F_{\rm pl} = \frac{\delta M}{b^2} - \frac{\delta Q_m^2 \sin\phi}{b^3}, \tag{6.6}$$

where the second term is resonant with the homogeneous solution, producing a secular (linearly growing) orbit correction. Solving the forced harmonic oscillator equations with boundary

conditions $u_1(0) = u_1'(0) = 0$ yields the first-order plasma corrections,

$$u_1^{(\delta M)} = \frac{\delta M(1-\cos\phi)}{b^2} \quad \text{and} \quad u_1^{(\delta Q)} = -\frac{\delta Q_m^2}{2b^3}(\sin\phi - \phi\cos\phi). \tag{6.7}$$

At second order, the plasma orbit corrections cross-multiply with the vacuum terms in $F'(u_0) = 6Mu_0 - 6Q_m^2u_0^2$, producing three additional contributions at orders $\delta M^2/b^2$, $\delta MQ_m^2/b^3$ and $\delta Q_m^4/b^4$. Combining the vacuum result from equation (5.8) with both first- and second-order plasma terms, the total plasma deflection angle consistent to second order reads

$$\hat{\alpha}_{\rm pl} = \hat{\alpha}_{\rm vac} + \frac{2\delta M}{b} - \frac{\pi\delta Q_m^2}{2\,b^2} + \frac{3\pi\delta M^2}{b^2} - \frac{40\delta MQ_m^2}{3\,b^3} + \frac{45\pi\delta Q_m^4}{32\,b^4} + \mathcal{O}(\delta^2, \delta\varepsilon, b^{-5}), \tag{6.8}$$

where $\hat{\alpha}_{\rm vac}$ is the vacuum deflection angle given by equation (5.8) and $\varepsilon = \alpha - \beta$. The first-order plasma terms $2\delta M/b$ and $-\pi\delta Q_m^2/(2b^2)$ agree with standard results for a uniform plasma medium [59,105]. The three second-order plasma–gravity cross-terms are new:

— $3\pi\delta M^2/b^2$: plasma enhances the post–post-Newtonian gravitational deflection;
— $-40\delta MQ_m^2/(3b^3)$: the combined plasma–charge correction opposes the bending; and
— $45\pi\delta Q_m^4/(32b^4)$: a higher-order dispersive–electromagnetic coupling.

Setting $Q_m = 0$ and $\delta = 0$ recovers the Schwarzschild vacuum limit with coefficient $15\pi/4$ [101], while setting only $\delta = 0$ recovers the vacuum result equation (5.8), confirming internal consistency. Numerical comparison with the exact orbit integral shows that including the second-order terms reduces the error by a factor of approximately 4.6 relative to the first-order result.

The plasma parameter $\delta = \omega_e^2/\omega_\infty^2$ introduces a frequency dependence: lower-frequency photons experience stronger plasma effects, leading to chromatic lensing signatures. The positive coefficient 3π of the $\delta M^2/b^2$ term indicates that plasma amplifies the gravitational contribution to the deflection, while the negative sign of $-40\delta MQ_m^2/(3b^3)$ shows that magnetic charge partially counteracts this amplification in the presence of plasma. Different astrophysical systems—magnetars, supermassive BHs or primordial BHs—may exhibit distinct chromatic lensing signatures depending on their charge-to-mass ratio, plasma density and observation frequency. Such frequency-dependent deflection signatures may, in principle, be probed through multiband radio observations, offering a potential observational window to constrain NLED couplings and plasma properties in strong-field environments [107].

Figure 13 presents the total deflection angle $\hat{\alpha}_{\rm pl}$ in a dispersive plasma environment for two representative magnetic charge values: (a) $Q_m = 0$ and (b) $Q_m = 1$. The heatmaps display the deflection angle as a function of the impact parameter b and the plasma parameter δ. For the uncharged case $Q_m = 0$, panel (a) recovers the Schwarzschild limit modified by plasma dispersion, showing the enhancement of the bending angle through the $2\delta M/b$ and $3\pi\delta M^2/b^2$ terms. Panel (b), corresponding to $Q_m = 1$, exhibits the combined influence of magnetic charge and plasma, where the negative mixed term $-40\delta MQ_m^2/(3b^3)$ partially offsets the plasma enhancement at intermediate impact parameters. The two panels collectively demonstrate that multifrequency lensing observations could in principle disentangle the gravitational, electromagnetic and dispersive contributions.

7. Conclusion

In this study, we explored the thermodynamic and optical properties of BHs described by the EEH NLED, with particular emphasis on quantum gravitational corrections and plasma-mediated lensing effects. By extending the standard Einstein–Maxwell framework with higher-order electromagnetic interactions encoded in the coupling constants (α, β), the EEH model captured strong-field QED effects that are otherwise inaccessible in classical gravity [108–112]. The resulting spacetime geometry, presented in equation (2.7), exhibited charge-dependent corrections proportional to Q_m^4/r^6 that influenced both the mass–radius relation given in

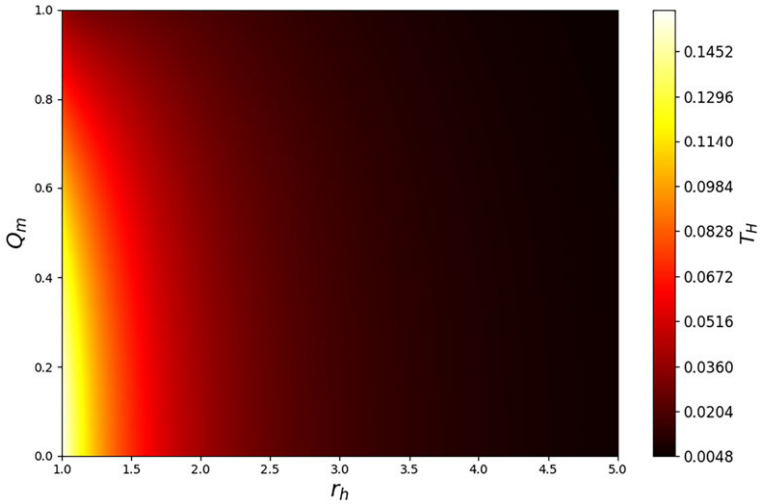

Figure 10. Hawking temperature T_H as a function of horizon radius r_h and magnetic charge Q_m for $M = 1$, $\alpha = 0.3$, $\beta = 0.1$. The colour intensity indicates the temperature magnitude, with darker regions corresponding to higher T_H. For fixed Q_m, the temperature increases as r_h decreases, reaching a maximum before the limit. Increasing Q_m at fixed r_h reduces the temperature due to the electromagnetic contribution $-Q_m^2/(2\pi r_h^3)$. The nonlinear EEH terms $\propto(\alpha - \beta)Q_m^4/r_h^7$ provide additional corrections that become prominent for large Q_m and small r_h, modifying the thermal spectrum compared to the RN BH.

equation (2.8) and the thermal behaviour of the BH. These modifications introduced distinctive horizon structures listed in table 1, revealing transitions between single root BH and non-extremal BH configurations depending on the interplay between magnetic charge and NLED couplings.

We employed a topological approach based on the Euler characteristic to derive the Hawking temperature in a coordinate-independent manner, as detailed in §2. This method, rooted in the GBT, provided an elegant geometric derivation that highlighted the deep connection between spacetime curvature and thermodynamic properties. The temperature formula obtained in equation (15) demonstrates how the nonlinear EEH terms $\propto(\alpha - \beta)Q_m^4/r_h^7$ systematically modified the thermal emission spectrum, with the isothermal profiles illustrated in figure 10 revealing the characteristic deformation of the near-horizon thermal structure induced by quantum electromagnetic corrections.

We further incorporated quantum gravitational effects through the GUP, which introduced a minimal measurable length l_p into the near-horizon dynamics. The modified uncertainty relation presented in equation (2.14) led to a suppression of the Hawking temperature at small scales, as captured by the GUP-corrected formula in equation (2.18). This modification suggested the possible existence of stable Planck-mass remnants at the final stages of evaporation, thereby bridging semiclassical and quantum gravity regimes. Figure 11 demonstrated that larger magnetic charges enhanced the remnant behaviour, indicating that both minimal length effects and magnetic coupling suppressed evaporation at small scales. Such a result offered valuable insight into how fundamental quantum corrections could alter BH evolution and potentially resolve the information paradox through remnant formation [113–116].

A direct comparison between quantum-corrected and uncorrected EEH BHs reveals several distinct physical features. First, the GUP modification suppresses the Hawking temperature by a factor $(1 - \lambda^2 l_p^2/4r_h^2)$, which amounts to 2.78% at $r_h = 1.5$ and increases sharply at smaller radii (table 2). This suppression drives the temperature to zero at $r_h = \lambda l_p/2$, implying stable remnant formation—a feature absent in semiclassical treatments. Second, the exponential entropy correction e^{-S_0} contributes 58% at $r_h = 0.5$ but becomes negligible (less than 0.01%) for $r_h > 1.5$ (table 3), demonstrating that quantum microstructure affects only near-Planck-scale horizons.

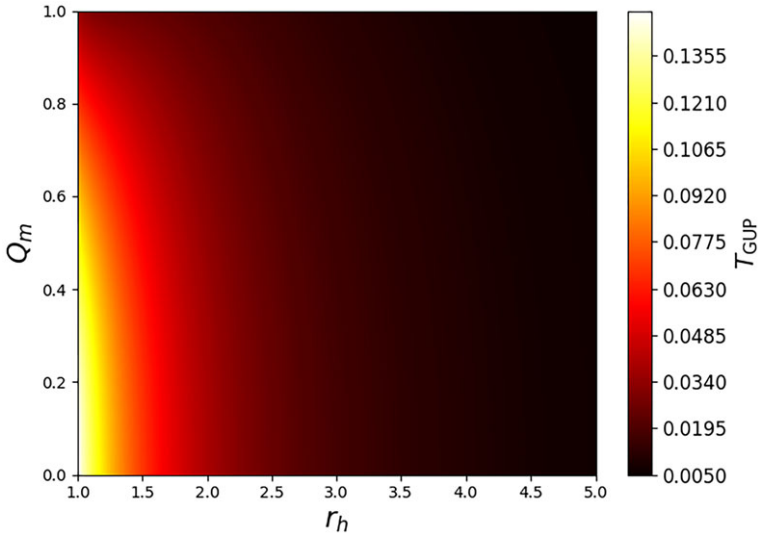

Figure 11. GUP-corrected Hawking temperature T_{GUP} versus horizon radius r_h and magnetic charge Q_m for $M = \lambda = 1$, $\alpha = 0.3$, $\beta = 0.1$, $l_p = 0.5$. The suppression factor $(1 - \lambda^2 l_p^2/4r_h^2)$ reduces the temperature compared to figure 10, with the effect becoming pronounced at small r_h. The temperature approaches zero as $r_h \to \lambda l_p/2 = 0.25$ (remnant radius), indicating that complete evaporation is prevented. Larger magnetic charges further reduce the peak temperature and enhance remnant stability. This behaviour represents a key prediction of quantum gravity: the existence of stable Planck-mass remnants that preserve information.

Third, the EC shifts the location of heat capacity divergences and modifies the swallow-tail structure in the Gibbs free energy, altering the critical behaviour compared to uncorrected BHs. These quantitative differences establish clear observational signatures that distinguish quantum-corrected EEH BHs from their classical counterparts.

By introducing ECs to the Bekenstein–Hawking entropy through the formula $S_{EC} = S_0 + e^{-S_0}$ given in equation (3.2), we examined their effect on the thermodynamic stability and phase behaviour of EEH BHs in §3. The corrected internal energy, Helmholtz free energy, pressure, enthalpy and Gibbs free energy were systematically derived in equations (3.5)–(3.11), revealing how quantum entropy modifications propagated through the entire thermodynamic structure. The heat capacity formula in equation (3.13) exhibited divergences marking second-order phase transitions, with figure 8 showing that the critical points shifted systematically with increasing magnetic charge. The Helmholtz free energy plot in figure 4 revealed that larger Q_m values altered the depth and position of local minima, tuning the phase transition threshold between small and large BH branches. The pressure profile in figure 5 demonstrated that EC smoothed classical singularities and enhanced stability at small horizons, while the Gibbs free energy in figure 7 exhibited characteristic swallow-tail structures indicative of first-order phase transitions in extended phase space.

The Joule–Thomson analysis presented in §4 further emphasized that quantum corrections affected the thermal response of the system under isenthalpic processes. The Joule–Thomson coefficient derived in equations (4.2)–(4.4) quantified the temperature change per unit pressure variation along constant-enthalpy trajectories, with figure 9 revealing multiple inversion points where the system switched between cooling and heating regimes. We found that these inversion points closely followed the heat capacity divergence structure, confirming that the underlying quantum corrections simultaneously regulated both isenthalpic and isothermal instabilities. This thermodynamic consistency underscored the robustness of the EC framework and demonstrated that the interplay between NLED, magnetic charge and quantum entropy modifications produced a unified phase structure accessible through multiple thermodynamic probes.

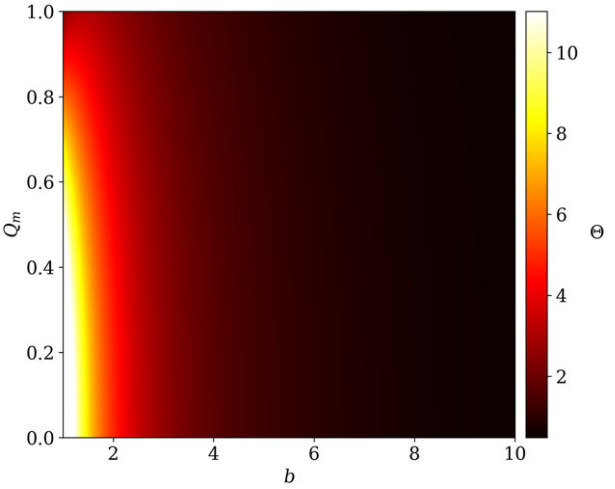

Figure 12. Vacuum deflection angle Θ versus impact parameter b and magnetic charge Q_m for $M = 1$, $\alpha = 0.3$, $\beta = 0.1$, computed via the Binet orbit equation to second order. Colour scale indicates Θ magnitude. For $b \lesssim 3M$, strong lensing dominates with steep Θ rise (photon sphere regime with multiple images or Einstein rings). At $b \gg M$, deflection follows $\Theta \approx 4M/b$. Increasing Q_m reduces Θ as magnetic field energy contributes a repulsive component. EEH corrections from $(\alpha - \beta)$ introduce modifications visible at $b \sim 5M$–$10M$.

The deflection of light around EEH BHs was analysed via the Binet orbit equation in both vacuum and plasma environments, as presented in §§5 and 6. This approach provided a self-consistent perturbative expansion to second order in M/b and Q_m^2/b^2, overcoming the well-known inconsistency of the Born approximation at second order [101,102]. In vacuum, the deflection angle Θ derived in equation (5.8) revealed the combined influence of mass, magnetic charge and NLED couplings on photon trajectories. The M^2/b^2 coefficient $15\pi/4$ reproduced the classical post–post-Newtonian Schwarzschild benchmark [101,103], while the mixed term $-16MQ_m^2/b^3$ and the Q_m^4/b^4 coefficient $105\pi/64$ emerged as new results specific to the magnetically charged EEH geometry. Figure 12 showed that increasing magnetic charge Q_m slightly decreased the bending magnitude, signifying that magnetic self-interaction weakened the effective optical curvature compared to the Schwarzschild limit. When plasma effects were incorporated through the frequency-dependent refractive index given in equation (6.1), the deflection angle acquired additional dispersive contributions quantified by the parameter $\delta = \omega_e^2/\omega_\infty^2$. The plasma deflection angle in equation (6.8) introduced three new second-order plasma–gravity cross-terms—$3\pi\delta M^2/b^2$, $-40\delta MQ_m^2/(3b^3)$ and $45\pi\delta Q_m^4/(32b^4)$—capturing the interplay between gravitational curvature, electromagnetic fields and plasma dispersion. Numerical verification against exact orbit integrals confirmed that the second-order expressions reduced the error by factors of approximately 5.4 (vacuum) and approximately 4.6 (plasma) relative to the first-order results. The heatmaps in figure 13 demonstrated that the plasma-induced deflection enhancement became more pronounced with increasing magnetic charge, leading to chromatic lensing signatures that could serve as observational diagnostics for constraining the EEH parameters through multifrequency radio observations.

Altogether, our results suggested that the interplay between NLED, quantum corrections and topological methods provided a consistent framework for understanding the microphysical and observational aspects of quantum-modified BHs. The EEH model emerged as a particularly rich theoretical laboratory where QED vacuum polarization effects, minimal length corrections and EC combined to produce distinctive signatures in both thermodynamic properties and lensing observables. The systematic deviations from classical predictions encoded in $\varepsilon = \alpha - \beta$, the magnetic charge Q_m, the GUP parameter λl_p^2 and the plasma dispersion parameter δ offered

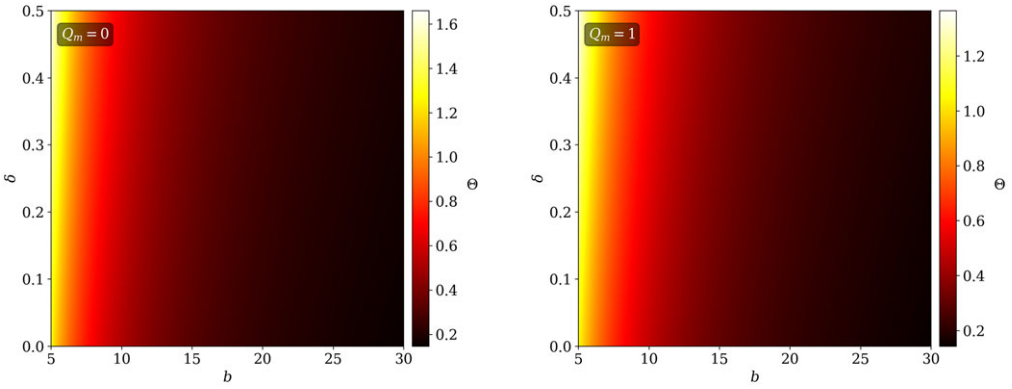

(a) $Q_m = 0$ (b) $Q_m = 1$

Figure 13. Deflection angle $\hat{\alpha}_{\rm pl}$ in a dispersive plasma environment as a function of impact parameter b and plasma parameter $\delta = \omega_e^2/\omega_\infty^2$ for $M = 1$, $\alpha = 0.3$, $\beta = 0.1$, computed via the Binet orbit equation to second order. (a) $Q_m = 0$ (Schwarzschild limit with plasma): plasma enhances the bending through the first-order $2\delta M/b$ term and the second-order $3\pi\,\delta M^2/b^2$ correction. (b) $Q_m = 1$ (magnetically charged EEH BH with plasma): the mixed term $-40\delta M Q_m^2/(3b^3)$ partially offsets the plasma enhancement at intermediate b, producing distinct chromatic signatures detectable through multiband radio observations.

multiple avenues for constraining these effects through astrophysical observations and laboratory analogue experiments [117–119].

Future extensions of this work may pursue several directions. First, the incorporation of an explicit anti-de Sitter (AdS) background would enable the analysis of phase coexistence structures and critical phenomena in the presence of a negative cosmological constant, potentially revealing van der Waals-like transitions and critical exponents analogous to ordinary thermodynamic systems. The AdS/conformal field theory (CFT) correspondence could further illuminate the holographic interpretation of the ECs and their connection to boundary CFT dynamics. Second, the extension to rotating EEH configurations described by Kerr–Newman-like solutions with NLED corrections would link lensing asymmetry with BH shadow observables. Third, the investigation of quasinormal modes and greybody factors in the EEH framework would probe the dynamical stability and spectral properties of these quantum-corrected BHs, with potential implications for gravitational wave astronomy and primordial BH detection [120–122].

Data accessibility. This article has no additional data.

Declaration of AI use. The AI-based language editing tool Writefull, integrated within the Overleaf platform, was partly used in auto-correction mode to identify and correct language errors during the writing process. No AI-assisted technology was used to generate scientific content, analyse or interpret data, or draw scientific conclusions. The authors reviewed and take full responsibility for the final content of the manuscript.

Authors' contributions. E.S.: formal analysis, investigation, resources, software, visualization, writing—original draft; I.S.: conceptualization, data curation, formal analysis, funding acquisition, investigation, methodology, project administration, resources, software, supervision, validation, visualization, writing—original draft, writing—review and editing.

Both authors gave final approval for publication and agreed to be held accountable for the work performed therein.

Conflict of interest declaration. We declare we have no competing interests.

Funding. No funding has been received for this article.

Acknowledgements. We thank the editor and the anonymous referees for their constructive comments and valuable suggestions, which have significantly improved the quality of this manuscript. We express our gratitude to EMU, TÜBİTAK, ANKOS and SCOAP3 for their scholarly support. İ.S. expresses gratitude for the essential contribution of COST Actions CA22113, CA21106, CA23130, CA21136 and CA23115 in promoting networking advancements.

References

1. Bekenstein JD. 1973 Black holes and entropy. *Phys. Rev. D* **7**, 2333–2346. (doi:10.1103/PhysRevD.7.2333)
2. Frolov VP, Fursaev DV, Zelnikov AI. 1997 Statistical origin of black hole entropy in induced gravity. *Nucl. Phys. B* **486**, 339–352. (doi:10.1016/S0550-3213(96)00678-5)
3. Sahan N, Sucu E, Sucu Y. 2025 Quantum phase transitions of Dirac particles in a magnetized rotating curved background: interplay of geometry, magnetization, and thermodynamics. *Phys. Dark Universe* **49**, 102005. (doi:10.1016/j.dark.2025.102005)
4. Hawking SW. 1976 Black holes and thermodynamics. *Phys. Rev. D* **13**, 191–197. (doi:10.1103/PhysRevD.13.191)
5. Bardeen JM, Carter B, Hawking SW. 1973 The four laws of black hole mechanics. *Commun. Math. Phys.* **31**, 161–170. (doi:10.1007/BF01645742)
6. Dunne GV. 2004 Heisenberg-Euler effective Lagrangians: basics and extensions. In *From fields to strings: circumnavigating theoretical physics. Ian Kogan memorial collection*, vol. 3, pp. 445–522. Singapore: World Scientific. (doi:10.1142/9789812775344_0014)
7. Bastianelli F, Davila JM, Schubert C. 2009 Gravitational corrections to the Euler-Heisenberg Lagrangian. *JHEP* **2009**, 086. (doi:10.1088/1126-6708/2009/03/086)
8. Gutierrez-Cano G, Niz G. 2025 Euler-Heisenberg black holes in Einsteinian cubic gravity. *Gen. Relativ. Gravit.* **57**, 8. (doi:10.1007/s10714-024-03339-0)
9. Bakopoulos A, Karakasis T, Mavromatos NE, Nakas T, Papantonopoulos E. 2024 Exact black holes in string-inspired Euler-Heisenberg theory. *Phys. Rev. D* **110**, 024014. (doi:10.1103/PhysRevD.110.024014)
10. Yajima H, Tamaki T. 2001 Black hole solutions in Euler-Heisenberg theory. *Phys. Rev. D* **63**, 064007. (doi:10.1103/PhysRevD.63.064007)
11. Mangut M, Özay G, İzzet S. 2024 On thermal fluctuations and quantum regularities of $F(R, G)$ gravity black holes with constant topological Euler density in nonlinear electrodynamics. *Phys. Scr.* **99**, 055005. (doi:10.1088/1402-4896/ad3504)
12. Alipour MR, Gashti SN, Pourhassan B, İzzet S. 2025 Reconciling the weak gravity and weak cosmic censorship conjectures in Einstein-Euler-Heisenberg-AdS black holes. (https://arxiv.org/abs/2504.03453)
13. Ahmed F, Al-Badawi A, İzzet S. 2025 Dynamics of test particles, QPOs and thermodynamics of charged Euler-Heisenberg AdS black holes with a cloud of strings and dark matter. (https://arxiv.org/abs/2509.12264)
14. Heisenberg W, Euler H. 2006 Consequences of Dirac theory of the positron. (https://arxiv.org/abs/physics/0605038).
15. Ruffini R, Wu YB, Xue SS. 2013 Einstein-Euler-Heisenberg theory and charged black holes. *Phys. Rev. D* **88**, 085004. (doi:10.1103/PhysRevD.88.085004)
16. Caneda PIC, Menezes G. 2021 Reduced quantum electrodynamics in curved space. *Phys. Rev. D* **103**, 065010. (doi:10.1103/PhysRevD.103.065010)
17. Gies H, Karbstein F. 2017 An addendum to the Heisenberg-Euler effective action beyond one loop. *J. High Energy Phys.* **2017**, 1–35. (doi:10.1007/JHEP03(2017)108)
18. Kong X, Ravndal F. 1998 Quantum corrections to the QED vacuum energy. *Nucl. Phys. B* **526**, 627–656. (doi:10.1016/S0550-3213(98)00364-2)
19. Balart L, Vagenas EC. 2014 Regular black holes with a nonlinear electrodynamics source. *Phys. Rev. D* **90**, 124045. (doi:10.1103/PhysRevD.90.124045)
20. Deka U, Chakraborty S, Kapadia SJ, Shaikh MA, Ajith P. 2025 Probing the charge of compact objects with gravitational microlensing of gravitational waves. *Phys. Rev. D* **111**, 064028. (doi:10.1103/PhysRevD.111.064028)
21. Walia RK. 2024 Exploring nonlinear electrodynamics theories: shadows of regular black holes and horizonless ultracompact objects. *Phys. Rev. D* **110**, 064058. (doi:10.1103/PhysRevD.110.064058)
22. Psaltis D. 2019 Testing general relativity with the Event Horizon Telescope. *Gen. Relativ. Gravit.* **51**, 137. (doi:10.1007/s10714-019-2611-5)
23. Sucu E, Sakalli I, Pourhassan B. 2025 Quantum corrections in thermodynamics of black holes modified by nonlinear electrodynamics and their observational signatures. *Int. J. Geom. Methods Mod. Phys.*, 2550243. (doi:10.1142/S0219887825502433)

24. Alestas G, Kazantzidis L, Nesseris S. 2022 Machine learning constraints on deviations from general relativity from the large scale structure of the Universe. *Phys. Rev. D* **106**, 103519. (doi:10.1103/PhysRevD.106.103519)
25. Kiefer C. 2005 The semiclassical approximation to quantum gravity. In *Canonical Gravity: From Classical to Quantum: Proceedings of the 117th WE Heraeus Seminar Held at Bad Honnef, Germany, 13–17 September 1993*, pp. 170–212. Berlin, Heidelberg, Germany: Springer. (doi:10.1007/3-540-58339-4_19)
26. Gursel H, Mangut M, Sucu E. 2025 Thermodynamics of Einstein-Euler-Heisenberg black holes with thermal fluctuations and nonlinear electromagnetic fields. *Classical Quantum Gravity* **42**, 135015. (doi:10.1088/1361-6382/ade7ea)
27. Robson CW, Di Mauro VL, Biancalana F. 2019 Topological nature of the Hawking temperature of black holes. *Phys. Rev. D* **99**, 044042. (doi:10.1103/PhysRevD.99.044042)
28. Zhang Y, Wei S, Liu Y. 2020 Topological approach to derive the global Hawking temperature of (massive) BTZ black hole. *Phys. Lett. B* **810**, 135788. (doi:10.1016/j.physletb.2020.135788)
29. Casadio R, Micu O, Nicolini P. 2014 Minimum length effects in black hole physics. In *Quantum aspects of black holes*, pp. 293–322. Cham, Switzerland: Springer. (doi:10.1007/978-3-319-10852-0_10)
30. Gecim G, Sucu Y. 2018 The GUP effect on tunneling of massive vector bosons from the $2+1$ dimensional black hole. *Adv. High Energy Phys.* **2018**, 7031767. (doi:10.1155/2018/7031767)
31. Alesci E, Bahrami S, Pranzetti D. 2019 Quantum gravity predictions for black hole interior geometry. *Phys. Lett. B* **797**, 134908. (doi:10.1016/j.physletb.2019.134908)
32. Gecim G, Sucu Y. 2017 The GUP effect on Hawking radiation of the $2+1$ dimensional black hole. *Phys. Lett. B* **773**, 391–394. (doi:10.1016/j.physletb.2017.08.053)
33. Sucu E, Sakallı İ. 2025 Quantum-corrected thermodynamics and plasma lensing of MOG black holes. *Proc. R. Soc. A* **481**, 20250251. (doi:10.1098/rspa.2025.0251)
34. Al Ghifari M, Ramadhan H, Alatas H, Sulaksono A. 2025 Bound on generalized uncertainty principle parameter from nuclear matter and slow rotating neutron stars. *Gen. Relativ. Gravit.* **57**, 1–33. (doi:10.1007/s10714-025-03457-3)
35. Gecim G, Sucu Y. 2020 Quantum gravity correction to Hawking radiation of the $2+$ 1-dimensional wormhole. *Adv. High Energy Phys.* **2020**, 1–10. (doi:10.1155/2020/7516789)
36. Luciano GG, Sekhmani Y. 2025 Generalized uncertainty principle mimicking dynamical dark energy: matter perturbations and gravitational wave data analysis. *Phys. Lett. B* **862**, 139315. (doi:10.1016/j.physletb.2025.139315)
37. Sucu E, Sakallı I. 2025 Nonlinear electrodynamics effects on the geometry, thermodynamics, and quantum dynamics of $(2+1)$-dimensional black holes. *Nucl. Phys. B* **1015**, 116894. (doi:10.1016/j.nuclphysb.2025.116894)
38. Chalavadi CC, Venkatesha V, Malik A. 2024 Exploration of GUP-corrected Casimir wormholes in extended teleparallel gravity with matter coupling. *Nucl. Phys. B* **1006**, 116644. (doi:10.1016/j.nuclphysb.2024.116644)
39. Ahmed F, Al-Badawi A, Sakallı İ, Bouzenada A. 2025 Quasinormal modes and GUP-corrected Hawking radiation of BTZ black holes within modified gravity frameworks. *Nucl. Phys. B* **1011**, 116806. (doi:10.1016/j.nuclphysb.2025.116806)
40. Sucu E, Sakallı İ. 2025 Scalar-tensor corrections and observational signatures of hairy black holes in Horndeski gravity. *High Energy Density Phys.* **56**, 101220. (doi:10.1016/j.hedp.2025.101220)
41. Wojnar A. 2024 Unveiling phase space modifications: a clash of modified gravity and the generalized uncertainty principle. *Phys. Rev. D* **109**, 024011. (doi:10.1103/PhysRevD.109.024011)
42. Gecim G, Sucu Y. 2017 Massive vector bosons tunnelled from the $(2+1)$-dimensional black holes. *Eur. Phys. J. Plus* **132**, 105. (doi:10.1140/epjp/i2017-11391-2)
43. Yang F. 2025 Generalized uncertainty principle models' multifaceted impact on black hole thermodynamics and entropy conservation during Hawking radiation. *Mod. Phys. Lett. A* **40**, 2550132. (doi:10.1142/S0217732325501329)
44. Tekincay C, Dernek M, Sucu Y. 2021 Exotic criticality of the BTZ black hole. *Eur. Phys. J. Plus* **136**, 222. (doi:10.1140/epjp/s13360-021-01168-7)
45. Tang M. 2024 Weak cosmic censorship conjecture and black hole shadow for black hole with generalized uncertainty principle. *Eur. Phys. J. C* **84**, 396. (doi:10.1140/epjc/s10052-024-12641-9)

46. Tekincay C, Gecim G, Sucu Y. 2021 Zitterbewegung particles tunneling from Reissner-Nordström AdS black hole surrounded by quintessence. *Europhys. Lett.* **135**, 31003. (doi:10.1209/0295-5075/ac1aac)
47. Battista E, Capozziello S, Errehymy A. 2024 Generalized uncertainty principle corrections in Rastall–Rainbow Casimir wormholes. *Eur. Phys. J. C* **84**, 1314. (doi:10.1140/epjc/s10052-024-13656-y)
48. Gecim G, Sucu Y. 2018 Quantum gravity effect on the Hawking radiation of charged rotating BTZ black hole. *Gen. Relativ. Gravit.* **50**, 152. (doi:10.1007/s10714-018-2478-x)
49. Li JL, Qiao CF. 2021 The generalized uncertainty principle. *Ann. Phys.* **533**, 2000335. (doi:10.1002/andp.202000335)
50. Gecim G, Sucu Y. 2018 Quantum gravity effect on the Tunneling particles from $2+1$-dimensional new-type black hole. *Adv. High Energy Phys.* **2018**, 8728564. (doi:10.1155/2018/8728564)
51. Sucu E, Sakallı İ, Sucu Y. 2026 Multi-spin particle tunneling and black hole thermodynamics: GUP-corrected zitterbewegung and exponentially modified entropy. *Phys. Lett. B* **875**, 140282. (doi:10.1016/j.physletb.2026.140282)
52. Ran JY, Wei JJ. 2024 Extragalactic test of general relativity from strong gravitational lensing by using artificial neural networks. *Phys. Rev. D* **109**, 043001. (doi:10.1103/PhysRevD.109.043001)
53. Chowdhuri A, Ghosh S, Bhattacharyya A. 2023 A review on analytical studies in gravitational lensing. *Front. Phys.* **11**, 1113909. (doi:10.3389/fphy.2023.1113909)
54. Bessa P. 2023 Strong gravitational lensing in Horndeski theory of gravity. *Phys. Rev. D* **108**, 024062. (doi:10.1103/PhysRevD.108.024062)
55. Sucu E. 2026 Quantum gravity corrections and plasma-induced lensing of magnetically charged black holes. *Nucl. Phys. B* **1022**, 117285. (doi:10.1016/j.nuclphysb.2025.117285)
56. Sucu E. 2026 Dirac particles tunnelling, barrow thermodynamics, and gravitational lensing in noncommutative-Finsler spacetimes. *Phys. Scr.* **101**, 075001 (doi:10.1088/1402-4896/ae414b)
57. Gibbons GW, Werner MC. 2008 Applications of the Gauss–Bonnet theorem to gravitational lensing. *Classical Quantum Gravity* **25**, 235009. (doi:10.1088/0264-9381/25/23/235009)
58. Tsupko OY, Bisnovatyi-Kogan GS. 2013 Gravitational lensing in plasma: relativistic images at homogeneous plasma. *Phys. Rev. D* **87**, 124009. (doi:10.1103/PhysRevD.87.124009)
59. Bisnovatyi-Kogan GS, Tsupko OY. 2010 Gravitational lensing in a non-uniform plasma. *Mon. Not. R. Astron. Soc.* **404**, 1790. (doi:10.1111/j.1365-2966.2010.16290.x)
60. Sucu E, Sakallı İ, Sert Ö, Sucu Y. 2025 Quantum-corrected thermodynamics and plasma lensing in non-minimally coupled symmetric teleparallel black holes. *Phys. Dark Universe* **50**, 102063. (doi:10.1016/j.dark.2025.102063)
61. Sarkar S, Sarkar N, Shah HH, Balo P, Rahaman F. 2025 Deflection angle of regular black holes in nonlinear electrodynamics: Gauss-Bonnet theorem, time delay, shadow, and greybody bound. *Phys. Lett. B* **870**, 139905. (doi:10.1016/j.physletb.2025.139905)
62. Sucu E, Sakallı İ. 2025 Astrophysical reality of black hole thermodynamics and dynamics: transformative influence of Hernquist dark matter distributions. *Phys. Dark Universe* **49**, 102051. (doi:10.1016/j.dark.2025.102051)
63. Sarkar S, Sarkar N, Dutta A, Rahaman F. 2024 Weak deflection angle by the Einstein–Cartan traversable wormhole using Gauss–Bonnet theorem with time delay. *Universe* **10**, 331. (doi:10.3390/universe10080331)
64. Sucu E, Sakallı İ. 2025 Exploring Lorentz-violating effects of Kalb-Ramond field on charged black hole thermodynamics and photon dynamics. *Phys. Rev. D* **111**, 064049. (doi:10.1103/PhysRevD.111.064049)
65. Ali R, Tiecheng X, Awais M, Babar R. 2025 Study of light deflection and shadow from a hairy black hole under the influence of the non-magnetic plasma. *Chin. J. Phys.* **94**, 416–430. (doi:10.1016/j.cjph.2025.01.023)
66. Sucu E, Sakallı İ. 2025 Charged regular black holes in quantum gravity: from thermodynamic stability to observational phenomena. *Eur. Phys. J. C* **85**, 989. (doi:10.1140/epjc/s10052-025-14726-5)
67. Al-Badawi A, Gogoi DJ, Sekhmani Y, Boshkayev K. 2025 Shadow and quasinormal modes of GUP corrected Grumiller black holes. *Nucl. Phys. B* **1015**, 116900. (doi:10.1016/j.nuclphysb.2025.116900)

68. Fathi M, Villanueva JR, Aguilar-Pérez G, Cruz M. 2024 Black hole in a generalized Chaplygin–Jacobi dark fluid: shadow and light deflection angle. *Phys. Dark Universe* **46**, 101598. (doi:10.1016/j.dark.2024.101598)
69. Al-Badawi A, Sekhmani Y, Rayimbaev J, Myrzakulov R. 2024 Shadows and quasinormal modes of black holes in the Einstein-*SU*(*N*) nonlinear sigma model. *Int. J. Mod. Phys. D* **33**, 2450043. (doi:10.1142/S0218271824500433)
70. Sucu E, Sakallı İ. 2025 Probing Starobinsky-Bel-Robinson gravity: gravitational lensing, thermodynamics, and orbital dynamics. *Nucl. Phys. B* **1018**, 116982. (doi:10.1016/j.nuclphysb.2025.116982)
71. Belhaj A, Sekhmani Y. 2022 Shadows of rotating quintessential black holes in Einstein–Gauss–Bonnet gravity with a cloud of strings. *Gen. Relativ. Gravit.* **54**, 17. (doi:10.1007/s10714-022-02902-x)
72. Fathi M, Sekhmani Y. 2025 Shadows aspect of rotating black holes in the Einstein-AdS *SU*(*N*)-nonlinear sigma model. *Eur. Phys. J. C* **85**, 1–25. (doi:10.1140/epjc/s10052-025-14153-6)
73. Aydiner E, Sucu E, Sakallı İ. 2025 Regular magnetically charged black holes from nonlinear electrodynamics: thermodynamics, light deflection, and orbital dynamics. *Phys. Dark Universe* **50**, 102164. (doi:10.1016/j.dark.2025.102164)
74. Chatterjee A, Ghosh A. 2020 Exponential corrections to black hole entropy. *Phys. Rev. Lett.* **125**, 041302. (doi:10.1103/PhysRevLett.125.041302)
75. Pourhassan B. 2021 Exponential corrected thermodynamics of black holes. *J. Stat. Mech.: Theory Exp.* **2021**, 073102. (doi:10.1088/1742-5468/ac0f6a)
76. Sakallı İ, Sucu Y, Sucu E. 2026 Zitterbewegung oscillations and GUP-induced quantum modifications of Yang-Mills black holes in perfect fluid dark matter. *Nucl. Phys. B* **1022**, 117216. (doi:10.1016/j.nuclphysb.2025.117216)
77. Biswas A. 2021 Joule-Thomson expansion of AdS black holes in Einstein Power-Yang-mills gravity. *Phys. Scr.* **96**, 125310. (doi:10.1088/1402-4896/ac2b42)
78. Cisterna A, Hu SQ, Kuang XM. 2019 Joule-Thomson expansion in AdS black holes with momentum relaxation. *Phys. Lett. B* **797**, 134883. (doi:10.1016/j.physletb.2019.134883)
79. Mo JX, Li GQ, Lan SQ, Xu XB. 2018 Joule-Thomson expansion of *d*-dimensional charged AdS black holes. *Phys. Rev. D* **98**, 124032. (doi:10.1103/PhysRevD.98.124032)
80. Barrientos J, Mena J. 2022 Joule-Thomson expansion of AdS black holes in quasitopological electromagnetism. *Phys. Rev. D* **106**, 044064. (doi:10.1103/PhysRevD.106.044064)
81. Yasir M, Lining T, Bamba K. 2025 Differential topology and micro-structure of black hole in Einstein–Euler–Heisenberg spacetimes with exponential entropy. *Phys. Dark Universe* **50**, 102128. (doi:10.1016/j.dark.2025.102128)
82. Yajima H, Tamaki T. 2001 Black hole solutions in Euler-Heisenberg theory. *Phys. Rev. D* **63**, 064007. (doi:10.1103/PhysRevD.63.064007)
83. Bakopoulos A, Karakasis T, Mavromatos NE, Nakas T, Papantonopoulos E. 2024 Exact black holes in string-inspired Euler-Heisenberg theory. *Phys. Rev. D* **110**, 024014. (doi:10.1103/PhysRevD.110.024014)
84. Sucu E, Övgün A. 2024 The effect of quark–antiquark confinement on the deflection angle by the NED black hole. *Phys. Dark Universe* **44**, 101446. (doi:10.1016/j.dark.2024.101446)
85. Miao YG, Wu YM. 2017 Thermodynamics of the Schwarzschild-AdS black hole with a minimal length. *Adv. High Energy Phys.* **2017**, 1–14. (doi:10.1155/2017/1095217)
86. Wang LH, Ma MS. 2022 Barrow black holes and the minimal length. *Phys. Lett. B* **831**, 137181. (doi:10.1016/j.physletb.2022.137181)
87. Mu B, Tao J, Wang P. 2020 Minimal length effect on thermodynamics and weak cosmic censorship conjecture in anti-de sitter black holes via charged particle absorption. *Adv. High Energy Phys.* **2020**, 1–9. (doi:10.1155/2020/2612946)
88. Nozari K, Fazlpour B. 2006 Generalized uncertainty principle, modified dispersion relations and the early universe thermodynamics. *Gen. Relativ. Gravit.* **38**, 1661–1679. (doi:10.1007/s10714-006-0331-0)
89. Pedram P, Nozari K, Taheri S. 2011 The effects of minimal length and maximal momentum on the transition rate of ultra cold neutrons in gravitational field. *J. High Energy Phys.* **2011**, 1–11. (doi:10.1007/JHEP03(2011)093)
90. Nozari K, Etemadi A. 2012 Minimal length, maximal momentum, and Hilbert space representation of quantum mechanics. *Phys. Rev. D* **85**, 104029. (doi:10.1103/PhysRevD.85.104029)

91. Sucu E, Sakalli I. 2025 AdS black holes in Einstein-Kalb-Ramond gravity: quantum corrections, phase transitions, and orbital dynamics. *Nucl. Phys. B* **1018**, 117081. (doi:10.1016/j.nuclphysb.2025.117081)
92. Bousso R, Miyaji M. 2024 Fluctuations in the entropy of Hawking radiation. *Phys. Rev. D* **109**, 026006. (doi:10.1103/PhysRevD.109.026006)
93. Calmet X, Kuipers F. 2021 Quantum gravitational corrections to the entropy of a Schwarzschild black hole. *Phys. Rev. D* **104**, 066012. (doi:10.1103/PhysRevD.104.066012)
94. Campos Delgado R. 2022 Quantum gravitational corrections to the entropy of a Reissner–Nordström black hole. *Eur. Phys. J. C* **82**, 272. (doi:10.1140/epjc/s10052-022-10232-0)
95. Rezaei AH, Nozari K. 2024 Joule–Thomson expansion in a mimetic black hole. *Sci. Rep.* **14**, 19475. (doi:10.1038/s41598-024-70308-7)
96. Mirza B, Naeimipour F, Tavakoli M. 2021 Joule-Thomson expansion of the quasitopological black holes. *Front. Phys.* **9**, 628727. (doi:10.3389/fphy.2021.628727)
97. Liang J, Mu B, Wang P. 2021 Joule-Thomson expansion of lower-dimensional black holes. *Phys. Rev. D* **104**, 124003. (doi:10.1103/PhysRevD.104.124003)
98. Sucu E, Sakallı İ, Sucu Y. 2026 Spin-dependent quantum corrections to Schwarzschild black hole thermodynamics with barrow entropy and GUP. *J. Geom. Methods Mod. Phys.*, 2650116. (doi:10.1142/S0219887826501161)
99. Wambsganss J. 1998 Gravitational lensing in astronomy. *Living Rev. Relativ.* **1**, 1–74. (doi:10.12942/lrr-1998-12)
100. Jafarzade K, Bazyar Z, Saghafi S, Nozari K. 2025 Optical signatures of Einstein–Euler–Heisenberg AdS/dS black holes in the light of event horizon telescope. *Eur. Phys. J. C* **85**, 869. (doi:10.1140/epjc/s10052-025-14521-2)
101. Epstein R, Shapiro II. 1980 Post-post-Newtonian deflection of light by the Sun. *Phys. Rev. D* **22**, 2947–2949. (doi:10.1103/PhysRevD.22.2947)
102. Keeton CR, Petters AO. 2005 Formalism for testing theories of gravity using lensing by compact objects. I. Static, spherically symmetric case. *Phys. Rev. D* **72**, 104006. (doi:10.1103/PhysRevD.72.104006)
103. Bodenner RE, Will CM. 2003 Deflection of light to second order: a tool for illustrating principles of general relativity. *Am. J. Phys.* **71**, 770–773. (doi:10.1119/1.1570416)
104. Rogers A. 2015 Frequency-dependent effects of gravitational lensing within plasma. *Mon. Not. R. Astron. Soc.* **451**, 17–25. (doi:10.1093/mnras/stv903)
105. Crisnejo G, Gallo E. 2018 Weak lensing in a plasma medium and gravitational deflection of massive particles using the Gauss–Bonnet theorem. A unified treatment. *Phys. Rev. D* **97**, 124016 (doi:10.1103/PhysRevD.97.124016)
106. Perlick V, Tsupko OY, Bisnovatyi-Kogan GS. 2015 Influence of a plasma on the shadow of a spherically symmetric black hole. *Phys. Rev. D* **92**, 104031. (doi:10.1103/PhysRevD.92.104031)
107. Weltman A*et al.*2020 Fundamental physics with the Square Kilometre Array. *Publ. Astron. Soc. Austral.* **37**, e002. (doi:10.1017/pasa.2019.42)
108. Schäfer A. 1996 QED in strong fields. *Nucl. Instrum. Meth. B* **119**, 48–54. (doi:10.1016/0168-583X(96)00276-5)
109. Ilderton A, Lundin J, Marklund M. 2010 Strong field, noncommutative QED. *SIGMA* **6**, 041. (doi:10.3842/SIGMA.2010.041)
110. Dunne GV. 2009 New strong-field QED effects at ELI: nonperturbative vacuum pair production. *Eur. Phys. J. D* **55**, 327–340. (doi:10.1140/epjd/e2009-00022-0)
111. Kim DH, Kim CM, Kim SP. 2024 Strong-field QED effects on polarization states in dipole and quadrudipole pulsar emissions. *Eur. Phys. J. C* **84**, 1322. (doi:10.1140/epjc/s10052-024-13662-0)
112. Heyl JS, Hernquist L. 1999 Nonlinear QED effects in strong field magnetohydrodynamics. *Phys. Rev. D* **59**, 045005. (doi:10.1103/PhysRevD.59.045005)
113. Adler RJ, Chen P, Santiago DI. 2001 The generalized uncertainty principle and black hole remnants. *Gen. Relativ. Gravit.* **33**, 2101–2108. (doi:10.1023/A:1015281430411)
114. Maziashvili M. 2006 Black hole remnants due to GUP or quantum gravity? *Phys. Lett. B* **635**, 232–234. (doi:10.1016/j.physletb.2006.03.009)
115. Gecim G, Sucu Y. 2018 Quantum gravity effect on the tunneling particles from Warped-AdS3 black hole. *Mod. Phys. Lett. A* **33**, 1850164. (doi:10.1142/S021773231850164X)
116. Gecim G, Sucu Y. 2019 Quantum gravity effect on the Hawking radiation of spinning dilaton black hole. *Eur. Phys. J. C* **79**, 882. (doi:10.1140/epjc/s10052-019-7400-5)

117. Bokulić A, Smolić I, Jurić T. 2021 Black hole thermodynamics in the presence of nonlinear electromagnetic fields. *Phys. Rev. D* **103**, 124059. (doi:10.1103/PhysRevD.103.124059)
118. Khoshrangbaf M, Akbarieh AR, Atazadeh K, Motavalli H. 2025 Accretion disk around the regular black holes with a nonlinear electrodynamics source. *New Astron.* **117**, 102354. (doi:10.1016/j.newast.2025.102354)
119. Du YZ, Li HF, Zhou XN, Guo WQ, Zhao R. 2022 Shadow thermodynamics of non-linear charged Anti-de Sitter black holes. *Chin. Phys. C* **46**, 122002. (doi:10.1088/1674-1137/ac87f1)
120. Kala S, Negi A, Nandan H. 2025 Quasinormal modes of a dyonic black hole in Einstein–Euler–Heisenberg theory. *J. Subatomic Part. Cosmol.* **3**, 100047. (doi:10.1016/j.jspc.2025.100047)
121. Jana S, Kar S. 2023 Shadows in dyonic Kerr-Sen black holes. *Phys. Rev. D* **108**, 044008. (doi:10.1103/PhysRevD.108.044008)
122. Zubair M, Raza MA, Abbas G. 2022 Optical features of rotating black hole with nonlinear electrodynamics. *Eur. Phys. J. C* **82**, 948. (doi:10.1140/epjc/s10052-022-10925-6)